Publications of the Astronomical Society of the Pacific, 134:015002 (26pp), 2022 January https://doi.org/10.1088/1538-3873/ac3cb4
© 2022. The Author(s). Published by IOP Publishing Ltd on behalf of the Astronomical Society of the Pacific (ASP). All rights reserved

OPEN ACCESS

iSHELL: a 1–5 micron $R = 80{,}000$ Immersion Grating Spectrograph for the NASA Infrared Telescope Facility

John Rayner[1], Alan Tokunaga[1], Daniel Jaffe[2], Timothy Bond[1,3], Morgan Bonnet[1], Gregory Ching[1], Michael Connelley[1], Michael Cushing[4], Daniel Kokubun[5], Charles Lockhart[1], William Vacca[6], and Eric Warmbier[1]
[1] Institute for Astronomy, University of Hawaii, 2680 Woodlawn Drive, Honolulu, HI, 96822, USA; jrayner@hawaii.edu
[2] Department of Astronomy, University of Texas, RLM 16.342, Austin, Texas, TX 78712, USA
[3] SLAC National Accelerator Laboratory (MS60/RM135), 2575 Sand Hill Rd. Menlo Park, California, CA 94025, USA
[4] Ritter Astrophysical Research Center, Department of Physics and Astronomy, University of Toledo, 2801 W. Bancroft St., Toledo, Ohio, OH 43606, USA
[5] Oceanit, 828 Fort Street Mall Suite 600, Honolulu, HI 96813, USA
[6] SOFIA-USRA, NASA Ames Research Center, MS N232-12, P.O. Box 1, Moffett Field, California, CA 940035, USA
Received 2021 September 8; accepted 2021 November 17; published 2022 January 11

Abstract

iSHELL is a 1.06–5.3 μm high spectral resolution spectrograph built for the 3.2 m NASA Infrared Telescope Facility (IRTF) on Maunakea, Hawaii. Dispersion is accomplished with a silicon immersion grating in order to keep the instrument small enough to be mounted at the Cassegrain focus of the telescope. The white pupil spectrograph produces resolving powers of up to about $R \equiv \lambda/\delta\lambda = 80{,}000$ ($0\farcs375$ slit). Cross-dispersing gratings mounted in a tiltable mechanism allow observers to select different wavelength ranges and, in combination with a slit wheel and Dekker mechanism, slit widths ranging from $0\farcs375$ to $4\farcs0$ and slit lengths ranging from $5''$ to $25''$. One Teledyne 2048×2048 HAWAII-2RG array is used in the spectrograph, and one Raytheon 512×512 Aladdin 2 array is used in a 1–5 μm slit viewer for object acquisition, guiding, and scientific imaging. iSHELL has been in productive regular use on IRTF since first light in 2016 September. In this paper we discuss details of the science case, design, construction and astronomical use of iSHELL.

Unified Astronomy Thesaurus concepts: High resolution spectroscopy (2096); Ground-based astronomy (686); Astronomical instrumentation (799); Astronomical detectors (84); Infrared astronomy (786); Infrared observatories (791)

1. Introduction

The NASA Infrared Telescope Facility (IRTF) is a 3.2 meter infrared telescope located at an altitude of approximately 13,600 feet near the summit of Maunakea on the island of Hawaii. The University of Hawaii (UH) operates IRTF under contract to NASA while NSF agrees to receive proposals for new facility instruments and support costs for observing programs of interest to NSF. Designed for maximum performance in the infrared, IRTF takes advantage of the high transmission, excellent seeing, minimal water vapor, and low thermal background that characterize the atmosphere above Maunakea.

IRTF is operated as a national facility. Through peer review of proposals, observing time on the telescope is open to the entire astronomical community. Approximately 50% of available observing time is dedicated to solar system mission support and planetary observations. The remaining time is assigned to non-solar system science. Following a proprietary period of eighteen months, data from IRTF facility instruments is publicly available on the Infrared Science Archive at the NASA Infrared Processing and Analysis Center (IPAC).[7]

The immersion grating echelle spectrograph, iSHELL, was planned as a replacement for CSHELL, which is a single-order echelle spectrograph that uses a single 256×256 InSb array (Tokunaga et al. 1990; Greene et al. 1993). Capitalizing on technological developments in spectrograph gratings and infrared arrays, iSHELL provides greatly improved capabilities over CSHELL. The use of a Teledyne 2048×2048 HAWAII-2RG (H2RG) array in the spectrograph combined with a cross-dispersed spectral format, increases the simultaneous wavelength coverage by about 50 times, and doubles the resolving power.

Fundamental to the design of iSHELL is the use of a silicon immersion grating (SIG) provided by Dan Jaffe's group at the University of Texas (UT) at Austin. Jaffe's group has invested much research and development effort into producing silicon immersion gratings for infrared spectrographs (Marsh et al.

Original content from this work may be used under the terms of the Creative Commons Attribution 3.0 licence. Any further distribution of this work must maintain attribution to the author(s) and the title of the work, journal citation and DOI.

[7] https://irsa.ipac.caltech.edu/Missions/irtf.html

2007; Wang et al. 2010; Gully-Santiago et al. 2012). By employing an immersion grating to reduce the collimated beam diameter, the resolving power is doubled to $R \equiv \lambda/\delta\lambda = 80{,}000$ while at the same time keeping the cryostat relatively compact and small enough to mount at the Cassegrain focus of the telescope (see Sections 2.2 and 4.3). If iSHELL were to be built using a conventional grating, the diameter of the collimated beam and the focal length of the spectrograph collimator would need to be over three times larger, roughly doubling the volume and mass of the instrument. The grating used in iSHELL is very similar to that first used in the IGRINS spectrograph (Park et al. 2014). IGRINS covers the 1.5–2.4 μm simultaneously in one exposure (i.e., "one shot") at $R = 45{,}000$ whereas iSHELL covers the 1.06–5.3 μm at about $R = 80{,}000$ in 17 settings. iSHELL provides the opportunity to characterize the SIG technology over a much wider wavelength range than possible with IGRINS.

2. Science Case and Instrument Design Drivers

As an IRTF facility instrument and a replacement for CSHELL, the instrument is required to fulfill the needs of a diverse community of users. iSHELL complements the facility 0.7–5.4 μm $R = 50$–2500 cross-dispersed spectrograph and imager SpeX (Rayner et al. 2003), and the 5–25 μm $R = 15{,}000$–$100{,}000$ visitor instrument TEXES (Lacy et al. 2002).

A number of key science cases were explored to capitalize upon the increased resolving power and much-increased one-shot wavelength range to develop instrument design drivers. The most important considerations are the interplay between R, one-shot wavelength range, and slit length. Higher R leads to a smaller one-shot wavelength range. Also, the longer the slit length the fewer the number of spectral orders that can be placed on the array and so this also reduces the one-shot wavelength range. Since only one immersion grating was available to the IRTF, a further important consideration is at what wavelength to match the free spectral range (FSR) to the width of the H2RG array. Higher spectral orders underfill the array, reducing one-shot wavelength coverage, while lower orders overfill the array, resulting in gaps in wavelength coverage.

2.1. Science Drivers for High Resolving Power

For *L*/*L*′-band observations of thick disks and comets, resolving powers of up to about 100,000 (3 km s^{-1}) are optimum because of the high line density and the need to discriminate these features against the rich telluric spectrum, even at the cost of reduced wavelength coverage. In comets intrinsic lines are unresolved (1–2 km s^{-1}) but the high resolving power results in better line to continuum ratio and the un-blending of comet lines. For measurements of optically thin disks using the fundamental CO transitions in the *M* band, resolving powers from 30,000 to 50,000 will measure gas kinematics over a range of radii, while resolving powers up to 100,000 are optimum for measuring bulk motions in proto-stellar cores through line profiles.

The ground-based detection of CH_4 in the atmosphere of Mars was done in the *L* band at $R \approx 40{,}000$ (Mumma et al. 2009) but higher resolving power and would help to better separate telluric features. Resolving powers up to 100,000 are optimum for observations of H_3^+ lines at L' in the upper atmosphere of Jupiter. The *M*-band window provides a wealth of information about the gas composition and tropospheric cloud structure of Jupiter and Saturn. In this case, wide one-shot wavelength coverage is preferred over the highest resolving powers. Long slits are also desired for spatial coverage on planets.

The deconvolution techniques used to detect the spectral signatures of exoplanet atmospheres ideally require both high resolving power to separate intrinsic lines and contaminating telluric features, and wide one-shot wavelength coverage to cover as many intrinsic lines as possible (e.g., Snellen et al. 2010).

Our simulations (see Figure 3 in Jones et al. 2008, with the simulations done by co-author William Vacca) find that the optimum resolving power is about 70,000 for radial velocity (RV) observations of cool stars in the *K*-band window of a heavy methane ($^{13}CH_4$) gas cell.

In the *J*, *H* and *K* bands where telluric absorption and the sky and telescope background continuum is much reduced, stellar science profits from increased one-shot wavelength coverage (more features, simultaneous line ratios) and improved sensitivity that results from working at lower resolving powers ($R \leqslant 50{,}000$).

Since only one immersion grating is used and given the key science cases, we chose to optimize iSHELL for 3–5 μm while assuring the best allowable performance at 1–2.5 μm.

2.2. The Resolving Power, Slit Width, and Sampling

Given the science cases, the immersion grating available to us, and the instrument size limitations, we have chosen a resolving power of $\geqslant$70,000 matched to the smallest practical slit width.

In Littrow configuration, the angular dispersion, A, of an immersion grating with refractive index, n, is given by

$$A \equiv \frac{d\beta}{d\lambda} = \frac{2n \tan\delta}{\lambda}$$

where λ is the wavelength, β is the angle of diffraction, and δ is the blaze angle of the grating (Schroeder 2000). It can also be shown (Schroeder 2000) that resolving power, R, is given by

$$R = \frac{\lambda A}{r\phi}\frac{d_1}{D}$$

where d_1 is the incident collimated beam diameter, r is the anamorphic magnification, ϕ is the slit width (radians), and D is the telescope diameter.

Therefore, since iSHELL operates very close to Littrow configuration

$$R = \frac{2d}{\phi D} n \tan\delta \quad (1)$$

where $r = 1$, and $d_1 = d$.

To achieve good optical efficiency at the desired resolving power of $R \geqslant 70{,}000$, the nominal slit width is set to $0\farcs375$ (0.209 mm normal to the incoming beam and physically 0.226 mm on the tilted slit) to match the best uncorrected seeing at IRTF, with a selection of wider slits available. The size of the available silicon substrates limited the collimated beam diameter to about $d = 30$ mm at most. R3 format ($\tan\delta = 3$) on silicon ($n = 3.4$) was the standard format used by UT who fabricated the grating for iSHELL in 2014. This results in an instrument small enough to mount at Cassegrain focus ($d < 25$ mm), and with good sub-pixel optical aberrations in the spectrograph (f/38.3 collimator). Increasing the slit width to improve the optical efficiency in more typical seeing for the same resolving power would mean either increasing the instrument size (larger d) or increasing the immersion-grating format ($\tan\delta$), neither of which were practical at the time. (UT can now make R4 gratings on 30 mm thick material). We chose $d = 22.0$ mm to give an un-aberrated resolving power of $R = 80{,}000$.

Nyquist (i.e., two-pixel) sampling of the slit width is the absolute minimum needed. Experience shows that sampling of greater than 2.5 pixels is required for good telluric division while sampling of greater than four pixels is optimum to measure the instrument profile for precision radial velocity observations and spectro-astrometry. Good telluric cancellation and precision radial velocity ($\sim 10\,\mathrm{m\,s^{-1}}$) observations are also requirements. Decreasing the sampling improves the sensitivity per resolution element in the detector read noise limited regime (1–2.5 μm) and it also increases the wavelength coverage per exposure. We find that a reasonable compromise is for a sampling of three pixels per smallest slit width ($0\farcs125$ per pixel in the dispersion direction).

2.3. Wavelength Coverage and Slit Length

Practical considerations require a trade-off of one-shot wavelength coverage with resolving power, slit length, spectral sampling, and finite array size (Rayner et al. 2012). Silicon has a short wavelength limit of about 1.05 μm at 80 K (see Section 4.3). At the time of construction, the best available large format infrared array was the 2048 × 2048 Hawaii-2RG, which is sensitive over the range ~0.7–5.4 μm. iSHELL covers the range 1.06–5.3 μm with the one-shot wavelength coverage dependent upon the selected cross-dispersing grating and the selected slit length.

The science cases indicate that iSHELL will be used predominantly to observe point sources at J, H, and K, and both point sources and extended objects at L, L' and M. A slit length of $15''$ is used at $LL'M$ to comfortably nod point sources within the slit and to simultaneously subtract sky, any scattered light, and the dark/bias signal, without the need for separate sky and dark/bias exposures and consequent loss of observing efficiency. At the resolving power of iSHELL the only sky background at JHK is from sky emission lines while at $LL'M$ the background is dominated by thermal emission from the telescope and sky (see Figure 1). At JHK sky emission lines cover about two percent of detector pixels while the non-thermal sky continuum is orders of magnitude fainter than the dark current. Since the dark/bias is stable, nodding along the slit is not needed at JHK. Consequently, we use a $5''$ slit at JHK. The use of a shorter slit at JHK allows more spectral orders to be placed on the array and consequently more one-shot wavelength coverage. This is important at these shorter wavelengths since the immersion grating works in high orders resulting in decreased FSR per order (FSR = λ/order number).

2.4. Spectral Calibration

To achieve the proposed science the data needs to be flat fielded (S/N > 1000) and wavelength calibrated ($<1\,\mathrm{km\,s^{-1}}$ for non-RV science, $<10\,\mathrm{m\,s^{-1}}$ for RV science). Calibration needs to done fast and efficiently and ideally at the telescope position of the science targets to allow for any flexure in the instrument. This is done with an instrument-mounted calibration unit comprising illumination optics, flat-field lamps (quartz-tungsten-halogen for 1–2.5 μm and a 2000 K back body lamp for 2.7–5.3 μm), and a low-pressure Th-Ar Hollow Cathode Lamp (HCL) for wavelength calibration (Engleman et al. 2003; Kerber et al. 2008). We use a heavy methane ($^{13}CH_4$) gas cell for RV calibration. The use of this isotopologue of methane shifts absorption features away from the more common telluric $^{12}CH_4$ absorption features. Telluric emission features (ATRAN model, Lord 1992) are used to replace the arc lamp for wavelength calibration at thermal wavelengths (>3 μm) where arc lines are more difficult to detect due thermal emission and increasing opacity in the quartz envelope of the lamp. Using telluric features, spectral stability is limited to about $\geqslant 25\,\mathrm{m\,s^{-1}}$ by bulk atmospheric motions along the line of site (e.g., Kerber et al. 2008). For non-RV science this limitation is insignificant compared to the spectral resolution of the narrowest slit ($3750\,\mathrm{m\,s^{-1}}$).

In principle, telluric OH emission lines can be used for wavelength calibration at 1–2.3 μm (e.g. McCaughrean 1988) but this requires integration times of several hundred seconds for adequate S/N (see Figure 1). Using the Th-Ar lamp is much more efficient at these shorter wavelengths.

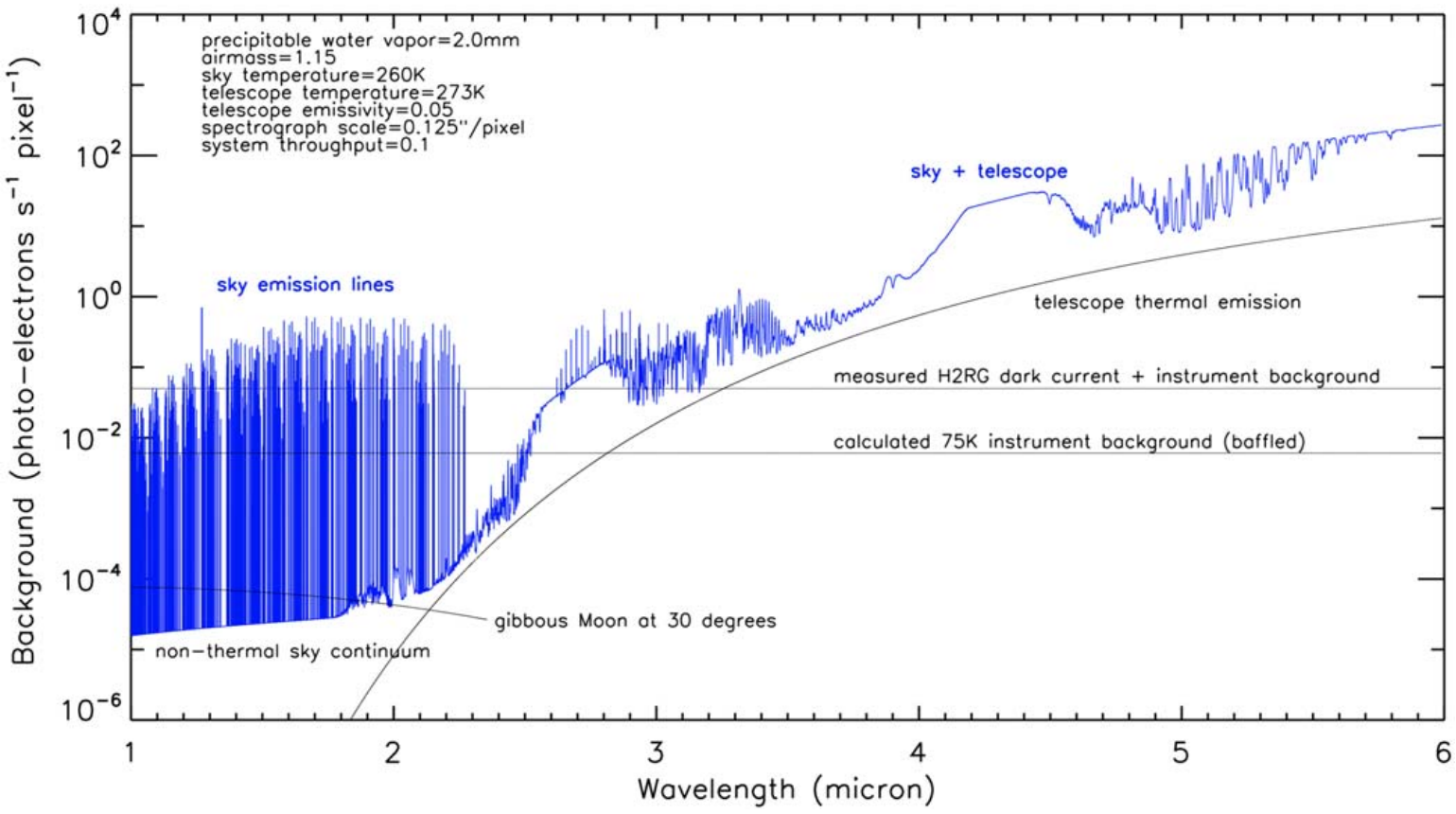


Figure 1. Modelled $R = 70{,}000$ background per pixel at the spectrograph H2RG array. Sky lines are from McCaughrean (1988) and the telluric spectrum is from ATRAN (Lord 1992). The non-thermal sky continuum is from Maihara et al. (1993). The brightness of the Moon is extrapolated from Sullivan & Simcoe (2012). iSHELL sensitivity is dark current and read noise limited at <2.5 μm where sky emission lines cover only a few percent of detector pixels, and background limited at >2.7 μm. A system throughput of 0.1 is a conservative estimate (see Table 2).

2.5. Observing Efficiency

Object acquisition and autoguiding is done with a 1–5 μm slit viewer similar to that used successfully in SpeX. For efficient use of observing time, target acquisition, positioning in the slit and IR guiding, setup must be done in less than about one minute. Due to iSHELL's high resolving power, most science targets appear relatively bright in the broad- and narrow-band filters available in the slit viewer. The ability to select an optimum filter from across the 1–5 μm range increases the flexibility of the instrument. Examples include guiding on point sources at *JHK*, daytime guiding on the thermal emission from comets at narrow-band *L*, to guiding on planetary features in the 3–5 μm range.

3. Optical Layout

Figure 2 shows a schematic layout of iSHELL. The iSHELL cryostat is mounted on IRTF's multiple instrument mount (MIM) at the Cassegrain focus of the telescope. In design the MIM is similar to a railroad car turntable and allows four large and fully cabled instruments to be mounted simultaneously on the telescope. It takes about 20 minutes to move an instrument on its mounting truck from the stow position and into the center (on-axis) position. Inside the cryostat are three major optical sub-assemblies: the foreoptics, the slit viewer, and the spectrograph. A spectral calibration unit is built into the cryostat-MIM interface box just above the cryostat entrance window.

3.1. Foreoptics

The f/38.3 beam from the telescope enters the cryostat through a 50 mm diameter CaF_2 window. Following the first fold mirror the beam comes to a focus at the telescope focal plane with a diameter of 42″, which is re-imaged without any demagnification onto the slit wheel by a collimator-camera system. The resulting slow f/38.3 beam into the spectrograph minimizes aberrations. A 10.0 mm diameter image of the telescope entrance pupil (the secondary mirror) is formed by a spherical collimating mirror (focal length 381 mm, diameter 50 mm) and the system cold stop is placed here. The 5° tilt of the collimator that is required for adequate separation of the input and exit beams still gives good image quality at the slits. It is necessary to place the cold stop before the slits since diffraction at the slits would otherwise blur the image of the pupil on a cold stop following the slits and result in higher backgrounds at thermal wavelengths. Located immediately behind the cold stop is a k-mirror image rotator, permitting slits to be aligned to any position angle on the sky. A BaF_2-LiF achromatic doublet lens images the collimated beam exiting the rotator onto the slit wheel.

3.2. Slit Viewer

Slit mirrors (see Section 4.6) in the slit wheel reflect the telescope focal plane (with an angular diameter of 42″) into the slit viewer optics. The slit mirrors are tilted 22°.5 with respect to the incoming beam to reflect the field into the slit viewer (see Figure 2). The 30.0 mm diameter (clear aperture 26 mm) of the slit mirrors set the size of the field available in the slit viewer. Due to the number of slit mirrors needed and space limitations, larger slit mirrors were not practical. A refractive collimator-camera re-images the slit field onto a Raytheon 512x512 InSb array with an image scale of 0″.10 per pixel. The collimator and

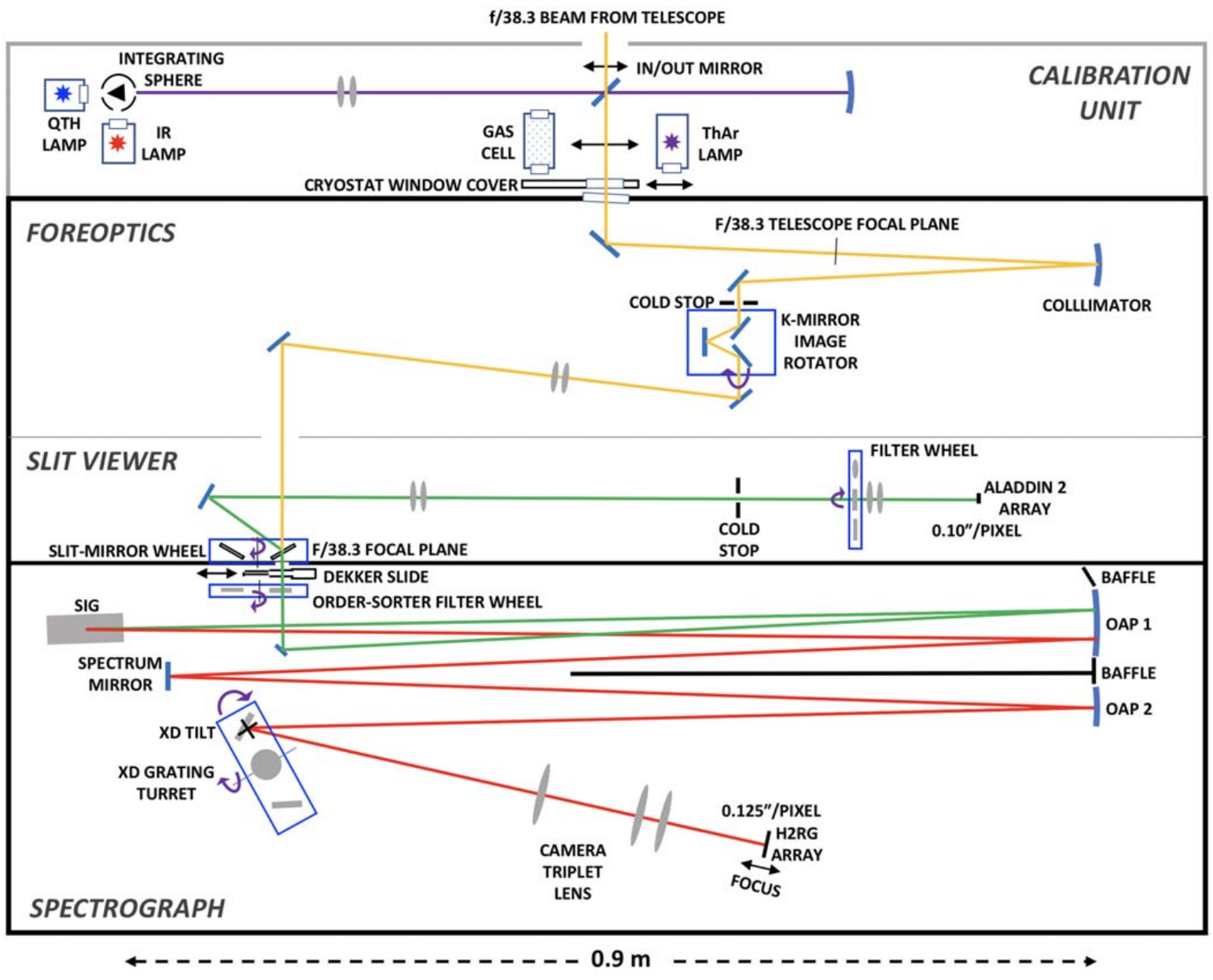


Figure 2. Schematic layout of iSHELL (approximately to scale). The cryostat optics consists of three major components: foreoptics, slit viewer, and white-pupil spectrograph. A spectral calibration unit is built into the box that mounts the cryostat to the telescope multiple instrument mount (MIM). There are eight cold mechanisms: k-mirror image rotator, slit-viewer filter wheel, slit-mirror wheel, Dekker slide, order-sorter filter wheel, cross-disperser (XD) grating turret (rotate and tilt), and spectrograph focus stage. The foreoptics and slit viewer are mounted on the opposite of side of a cold optical bench to the spectrograph. Important optical elements include the silicon immersion grating (SIG) and the aluminum off-axis parabolas (OAPs). In this view the layout is shown unfolded for clarity.

camera lenses are both BaF_2-LiF achromatic doublets. The collimator doublet lens collimates the beam and forms a 3.5 mm diameter pupil image where a second oversized cold stop is placed. An eight-position filter wheel containing a selection of 25 mm diameter filters is located 100 mm behind the pupil image. A CaF_2 lens sandwiched together with a narrow-band *L* filter in the filter wheel is used to image the entrance pupil for aligning the cryostat by examining the image of the telescope secondary mirror conjugated at the foreoptics cold stop and slit-viewer stop. Immediately following the filter wheel a camera doublet lens images the field onto the slit viewer array.

3.3. Spectrograph

A modified version of the white pupil design originally developed by Baranne (1972) is used in the spectrograph. This has the advantage of minimizing the tilt of the SIG needed to clear the incoming beam, allowing the echelle grating to operate more efficiently. In addition, locating the cross-dispersing (XD) gratings at the second pupil minimizes their size and maximizes the number that can be used, thereby increasing the number of spectral formats.

The f/38.3 beam from the foreoptics enters the spectrograph at the slit wheel. The slit mirrors are gold-coated substrates with a slit aperture lithographically applied to the front side of a CaF_2 substrate. Four slit-mirrors with slit widths of $0\farcs375$, $0\farcs75$, $1\farcs50$ and $4\farcs00$ respectively, and $30''$ (16.7 mm) long, are all mounted in the slit wheel together with a mirror (no slit). A slit Dekker slide located 1 mm behind the slit wheel allows slit lengths of $5''$, $15''$, and $25''$ to be selected (see Table 1). An eight-position order-sorting filter wheel follows the slit Dekker.

Following the order-sorter filter wheel, the beam is folded and collimated at the first off-axis parabola (OAP1). The R3 SIG is located close to the 22.0 mm diameter pupil formed by OAP1. The SIG is physically tilted by $1\fdg025$ ("gamma" angle) in the out-of-plane grating direction so that the dispersed beam is directed back towards OAP1 (the effective tilt in immersion

Table 1
List of iSHELL Spectral Observing Modes

Mode	Wavelength coverage (μm)	Order sorter	XD tilt (degrees)	Slit length (arcsec)	XD (line/mm)	Blaze wavel. (μm)	Blaze angle (deg.)	Orders covered (approx.)
J0	1.065–1.165	J_{OS}	51.3	5.0	1200	1.10	41.3	505–455
J1	1.11–1.22	J_{OS}	53.8	5.0	1200	1.10	41.3	481–436
J2	1.20–1.30	J_{OS}	58.3	5.0	1200	1.10	41.3	442–405
J3	1.27–1.36	J_{OS}	61.8	5.0	1200	1.10	41.3	416–386
H1	1.48–1.67	H_{OS}	44.0	5.0	720	1.90	43.1	354–314
H2	1.55–1.74	H_{OS}	45.7	5.0	720	1.90	43.1	338–300
H3	1.64–1.82	H_{OS}	48.1	5.0	720	1.90	43.1	319–287
K1	1.94–2.23	K_{OS}	40.5	5.0	497	2.25	34.0	268–232
K2	2.09–2.38	K_{OS}	43.0	5.0	497	2.25	34.0	249–219
K3	2.26–2.55	K_{OS}	45.9	5.0	497	2.25	34.0	230–205
Kgas	2.18–2.47	K_{OS}	44.5	5.0	497	2.25	34.0	240–212
L1	2.74–3.02	L_{OS}	50.0	15.0	450	3.10	45.0	189–172
L2	2.96–3.24	L_{OS}	53.9	15.0	450	3.10	45.0	175–160
L3	3.20–3.48	L_{OS}	58.5	15.0	450	3.10	45.0	161–149
Lp1	3.28–3.66	L_{OS}	48.0	15.0	360	3.70	42.0	158–142
Lp2	3.57–3.95	L_{OS}	52.3	15.0	360	3.70	42.0	144–132
Lp3	3.83–4.18	L_{OS}	52.3	15.0	360	3.70	42.0	135–125
Lp4	3.83–4.14	L_{OS}	55.7	25.0	360	3.70	42.0	133–125
M1	4.52–5.25 s	M_{OS}	40.4	15.0	210	5.0	31.7	113–98
M2	4.52–5.25 l	M_{OS}	40.4	15.0	210	5.0	31.7	113–98

is $1.025/n$ degrees). The beam from OAP1 then forms an in-focus dispersed image of the slit at the "spectrum mirror". This is a fused silica flat mirror with a protected silver reflection coating (optical surface 190.0 mm × 25.0 mm, substrate 31.8 mm thick). At OAP2 the beam from the spectrum mirror is re-collimated and forms a second "white" pupil image close to the cross dispersing (XD) grating. The XD gratings are not located exactly at the pupil to allow space for the grating turret. The OAPs are diamond-turned aluminum mirrors with off-axis angles of 3°.0 (see Section 4.5).

Gratings in the XD wheel diffract the beam into the spectrograph camera lens and the camera images the spectrum onto the 2048 × 2048 H2RG array. The camera is a BaF_2-ZnS-LiF three-element lens. Each lens is about 100 mm in diameter and all the surfaces are spherical. The XD wheel contains eight gratings. Individual gratings cover the *J*,*H*,*K*,*L*, *L′*, or *M* bands, and the grating blaze angle of a particular grating depends upon the band and the required slit length. Gratings are selected by rotating the XD wheel. The wheel is then tilted by a second mechanism about an axis through the grating to move spectral orders up and down the array to select the desired wavelength range. The wheel is designed for tilts in the range ±5°. The list of the gratings occupying the XD wheel and the resulting spectral formats is given in Table 1. Example spectral formats are illustrated in Figure 3. (All the spectral formats are illustrated in the online instrument manual[8]). Any order may be placed in the center of the array although the facility data reduction tool, Spextool (see Section 7), only extracts the modes listed in Table 1. The XD gratings are all replicas (fabricated using master gratings). Other wavelength settings require custom spectral extraction.

The optical design was done in ZEMAX.[9] Figure 4 shows the ZEMAX raytrace of the spectrograph.

3.4. Calibration Unit

A spectral calibration unit is built into the cryostat/MIM interface box. It consists of illumination optics, integrating sphere, and flat field and arc lamps (see Figure 2). The illumination optics, consisting of spherical mirror and BaF_2-LiF achromatic doublet lens, reimage the exit aperture of the integrating sphere onto the telescope focal plane inside the cryostat and also project a matched and uniform pupil onto the immersion grating, where the telescope pupil is conjugated. Wavelength calibration is done with a low-pressure Th-Ar lamp, and heavy methane gas cell ($^{13}CH_4$) for RV calibration, and flat-field calibration with a quartz-tungsten-halogen (QTH) lamp and a blackbody lamp. Translation stages are used to select the lamps and insert the cryostat window cover.

[8] http://irtfweb.ifa.hawaii.edu/~ishell/observer/
[9] https://zemax.com

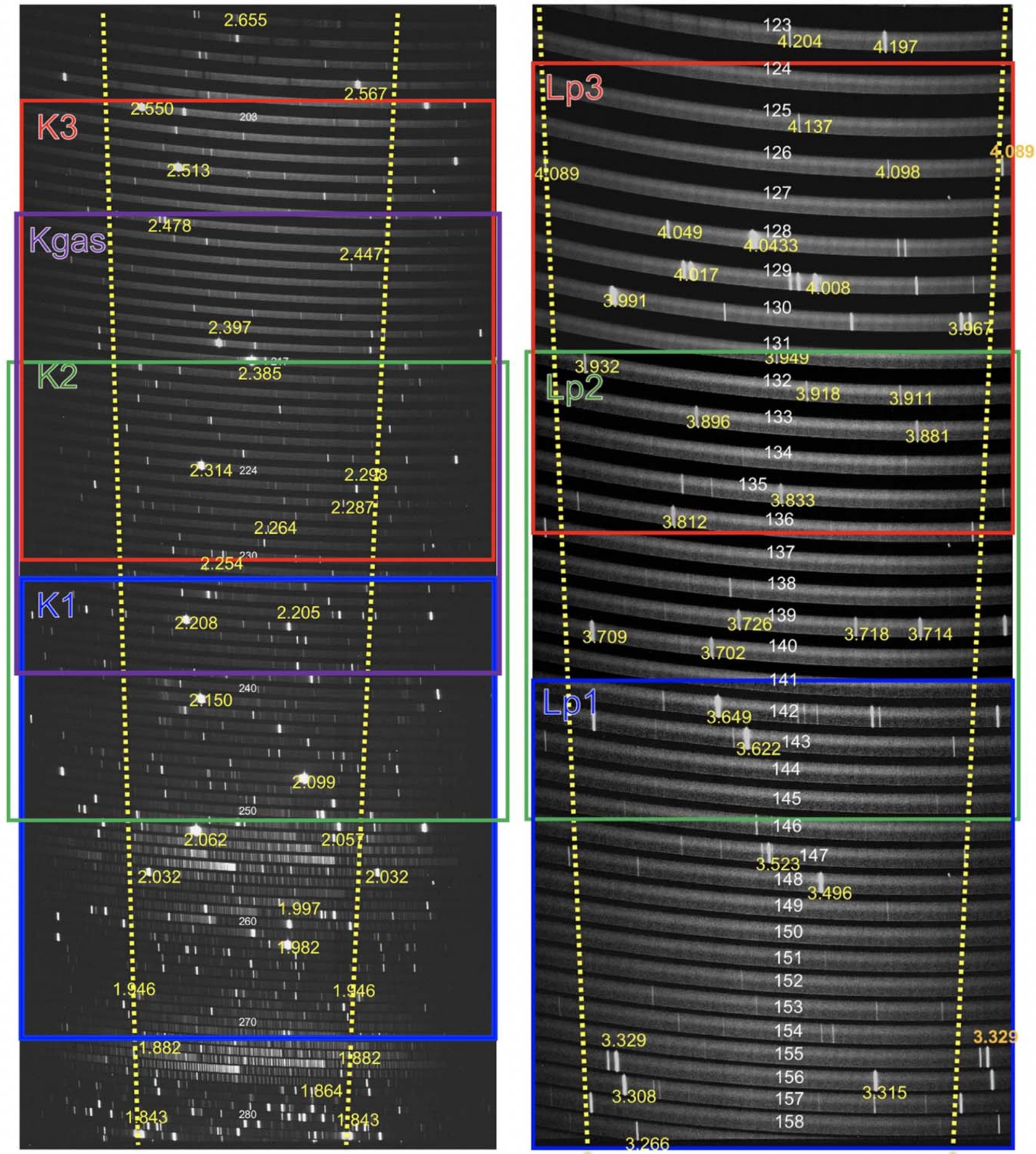


Figure 3. Th-Ar lamp exposures of the *K* (left) and *Lp* (right) spectral modes (see Table 1). The slit length is 5″ and 15″ respectively. Individual spectral images are shown mosaicked together in these views. The colored boxes indicate the one-shot wavelength coverage. Th-Ar line identifications are in microns (the decimal point indicates the exact location). Note the line contamination by the ThO_2 cathode at about 1.9 and 2.0 μm. The free spectral range (FSR) is shown by the yellow dashed lines. The FSR is matched to the H2RG array width at 4.2 μm in the *Lp* mode and underfills the array in the *K* mode. Both the *K* and *Lp* images are equal integration time arc lamp on minus arc lamp off exposures. The uneven background in the *Lp* mode is due to the difficulty of accurately subtracting thermal emission from the arc lamp.

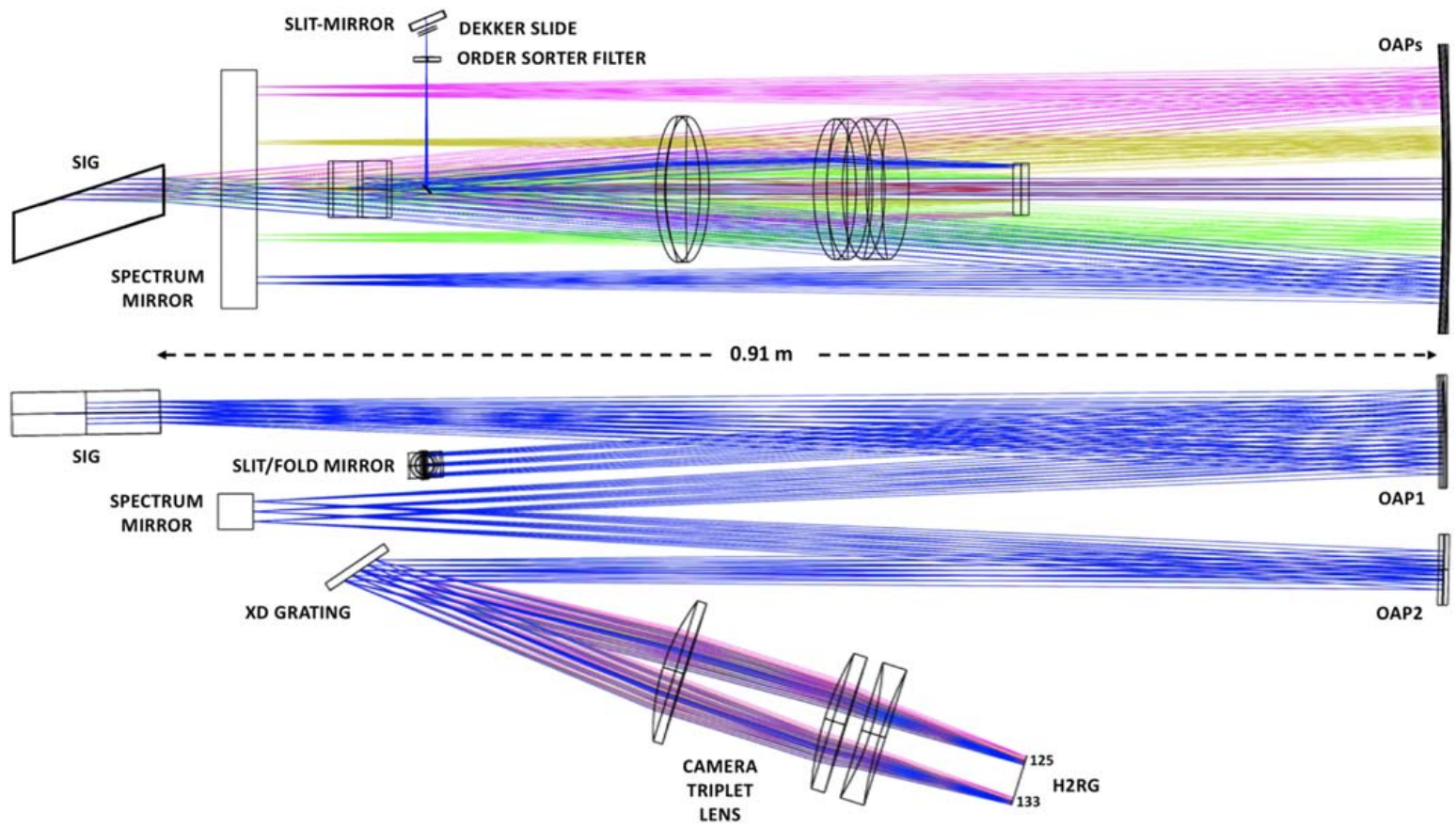


Figure 4. ZEMAX raytrace of the spectrograph *Lp4* mode, spectral orders 125 and 133 (see Table 1), 25_2 long slit. The longest and shortest wavelengths in each order are colored mauve (4.14 μm) and blue (3.83 μm) respectively. In this figure the view of the spectrograph optics from above (as seen from the telescope) is shown at the top and the side view is shown at the bottom. An image of the cross-disperser grating turret, spectrum mirror and SIG is shown in Figure 13. An image of the side view of the entire spectrograph is shown in Figure 16.

4. Optical Design and Fabrication

4.1. Optical Tolerancing

The low-frequency optical surface spatial errors (0.001–0.01 μm^{-1}) that affect the core of the image profile were analysed using the standard ZEMAX tolerancing parameters (e.g., thickness, radius, decentration, tilt, runout, surface irregularity, refractive index). Mid-frequency (0.01–1 μm^{-1}) and high-frequency optical surface spatial errors (>1 μm^{-1}—roughness, the source of scattered light) were analysed using a Power Spectrum Density function method (Stover 1990). For details of the iSHELL analysis and resulting optical specifications see Rayner et al. (2016).

The science requirement is for a spectrograph resolving power $R \equiv \lambda/\delta\lambda \geqslant 70{,}000$, where spectral resolution $\delta\lambda$, the smallest resolvable wavelength, is taken as the Full Width at Half Maximum (FWHM). In iSHELL the aberration-free diffraction-limited resolving power of $R = 80{,}000$ at 2.2 μm is matched to three pixels. R is also slightly dependent upon wavelength due to the 3% decrease in the refractive index of silicon from 1.1 to 5.3 μm (see Equation (1)). Using a Monte Carlo analysis and industry standard tolerances, 90% of the trials gave worst-case geometric 50% encircled energy dispersion widths better than 1.1 pixels. When added in quadrature with the diffraction-limited width of three pixels the FWHM is 3.2 pixels, equivalent to $R = 75{,}000$.

In fact, the measured resolving power matched to the narrowest slit ($0\farcs375$) is about $R = 80{,}000$ at 1–3 μm and about $R = 88{,}100$ at 5 μm (see Section 8). The reason for the slightly higher resolving powers is probably due a combination of better than expected optical performance, some uncertainty in the as-built geometrical optical parameters (see Equation (1)), and the effects of diffraction (see Section 4.2).

The dispersion, and therefore the resolving power, also changes across spectral orders as a function of the angle of diffraction for a fixed angle of incidence at the grating (e.g., Schroeder 2000). The effect becomes larger with increasing blaze angle and is therefore more significant in large format echelle grating spectrographs like iSHELL ($\tan\delta = 3$, see Equation (1)). At J, K and M, the variations across the FSR are about $R \pm 2\%$, $R \pm 4\%$ and $R \pm 8\%$, with respect to R at the center of the array respectively, with R increasing with wavelength across the order.

4.2. Effects of Diffraction

Diffraction at the narrowest slit broadens the image of the entrance pupil imaged through the slit. This image is projected onto the SIG. The effect is most significant at 5 μm (see Figure 5). The increased number of grating lines illuminated compared to the projected geometrical pupil (see Equation (1)) is consistent with the higher resolving power measured at 5 μm (see Section 8).

It is necessary to place the cold stop in front of the slits since diffraction would otherwise blur the image of the pupil on a cold stop following the slits and result in higher backgrounds at thermal wavelengths.

By design, iSHELL's resolving power is limited by the projected slit width ("spectral purity") onto the detector. The intrinsic resolving power due to the grating is much higher

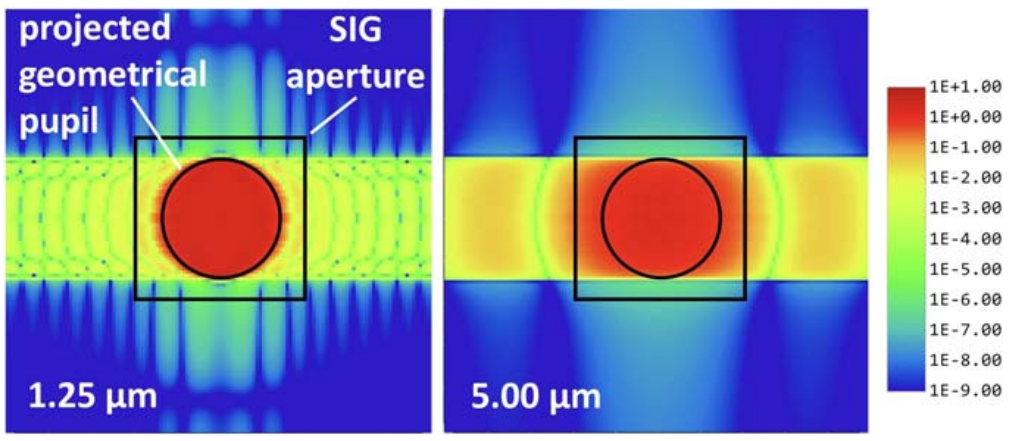


Figure 5. The effect of diffraction at the $0\farcs375$ (209 μm) slit on the pupil image projected onto the SIG. The pupil image at 5.00 μm is significantly broadened compared to that at 1.25 μm, resulting in higher resolving power due to the increased number grooves illuminated. Diffraction is much reduced in the direction along the slit (5″ at 1.25 μm and 15″ at 5.0 μm). Flux outside the SIG aperture does not reach the grating. Modelling of diffraction was done with the Physical Optics Propagation package in ZEMAX.

($R = \textit{spectral order} \times \textit{total number of lines}$ from Schroeder 2000) and is not the limitation. The spectral line spread function (i.e., the instrument profile) is effectively the convolution of the slit width with the monochromatic line profile from the grating. For a slit spectrograph the measured FWHM of the spectral line spread function is used to characterize the spectral resolution ($\delta\lambda$, Robertson 2013).

Where possible, optical element apertures are oversized compared to the geometrical beam sizes to minimize the effects of diffraction. The limiting aperture is the SIG entrance/exit face due to the limited disk size (about 30 mm). The FWHM of the instrument profile is little affected but diffraction at the SIG entrance/exit face at 5 μm does put slightly more flux into the wings of the instrument profile than ideal.

4.3. Silicon Immersion Grating (SIG)

The silicon immersion grating used in iSHELL was built and provided by Dan Jaffe's group at UT. Fabrication of the UT SIGs are detailed in the series of papers by Marsh et al. (2007), Wang et al. (2010) and Gully-Santiago et al. (2012). Briefly the steps are orienting, cutting, cleaning and polishing a 100 mm diameter by 30 mm thick disk of high resistivity Si, photolithography and etching to fabricate the grating surface, cutting the Si disk to the required shape, followed by anti-reflection coating the entrance face, and depositing a gold reflection coating on the grooved surface. iSHELL's SIG is shown in Figure 6 and its mount in Figure 7.

In a white pupil spectrograph, the grating tilt required to avoid beam collisions is only about one degree. This means that the loss of grating efficiency due to shadowing the grating grooves is not significant and so the grating can be illuminated in either near-Littrow or pseudo-Littrow orientation (see Schroeder 2000). We chose to illuminate the SIG in pseudo-Littrow mode with a gamma angle of $1\fdg025$ for two reasons. First, the resulting two-degree tilt of the spectral lines with respect to detector columns leads better sampling of telluric

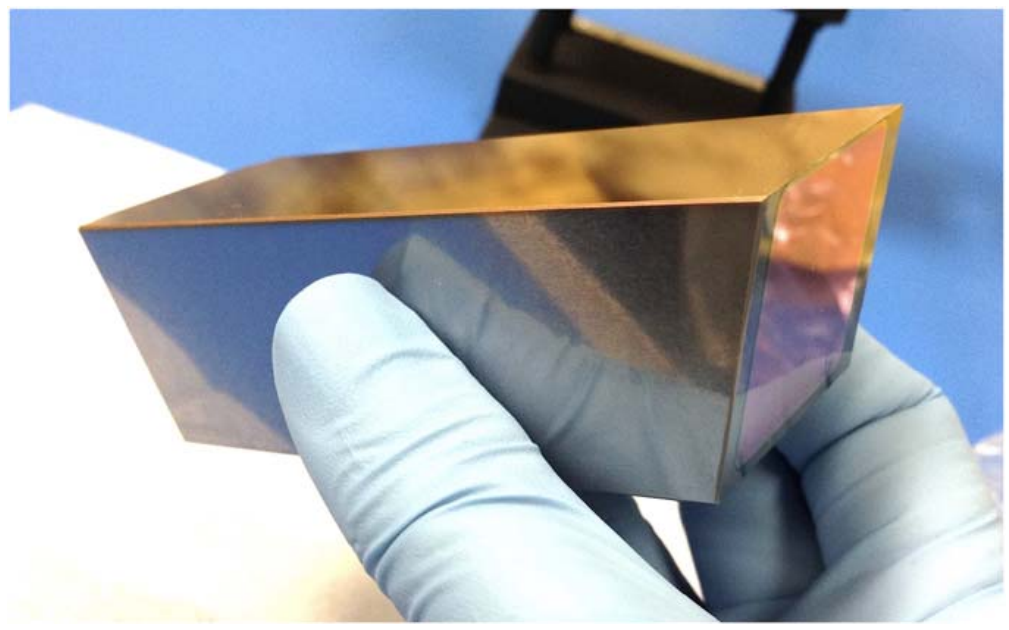


Figure 6. The silicon immersion grating fabricated for iSHELL. The 105 mm long grating surface is at the top and the anti-reflection coated 35.0 mm (vertical) × 30.5 mm entrance face is at the right.

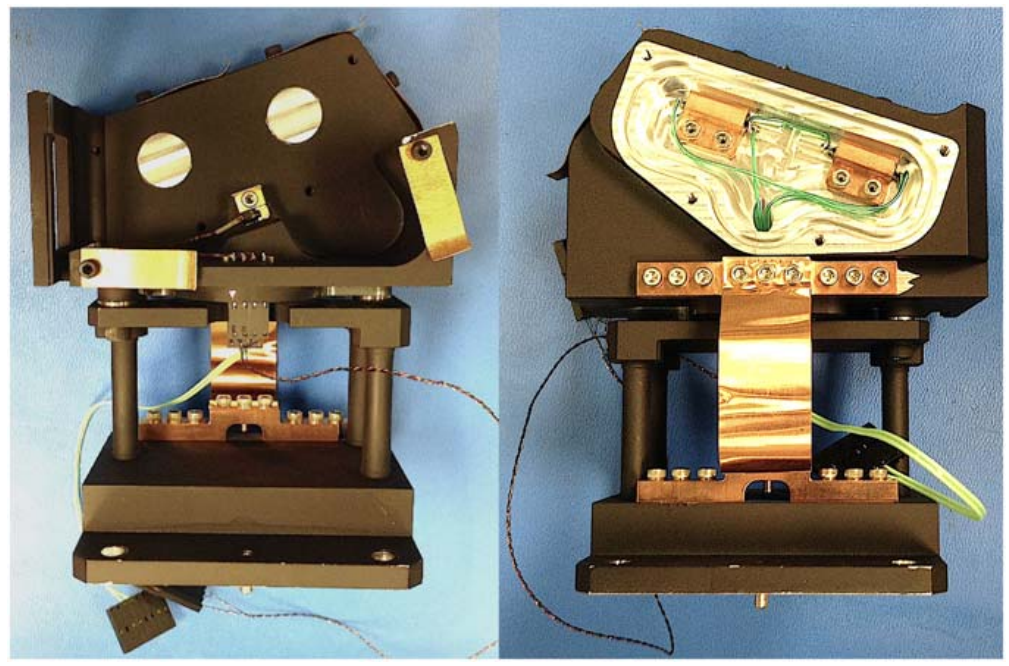


Figure 7. Silicon immersion grating mount and temperature control. Three rigid fiber-glass legs thermally isolate the mount from the cold optical bench. Resistor heaters embedded in the back of the aluminum mount (right) and copper foils form a thermal potentiometer controlled with feedback from a temperature diode mounted just below the two circular mounting pads (left). The mount temperature is controlled to 80.00 ± 0.02 K

features and therefore better sky subtraction (Kelson 2003). Second, pseudo-Littrow orientation removes the possibility of the so-called picket fence grating ghost (Tull et al. 1995).

The entrance/exit face of the SIG is also wedged by $0\fdg8$ in the same sense as the gamma angle to steer the un-dispersed ghost reflection away from the optical path and onto a baffle to the side of OAP1 (see Figures 2 and 8). The wedge also refracts internal reflections in the SIG away from the optical path.

We used the UT standard R3 ($\tan\delta = 3$) grating format. A groove width of 80.0 μm (12.5 lines/mm) is set by the requirement for the FSR to span the 2048 pixel-width of the array (with a 50 pixel border) at 4.15 μm. For $R = 80{,}000$ and three-pixel sampling, this sets the order number and thence the groove width. With only one SIG available to IRTF at the time, this was a compromise between overfilling the array at M and

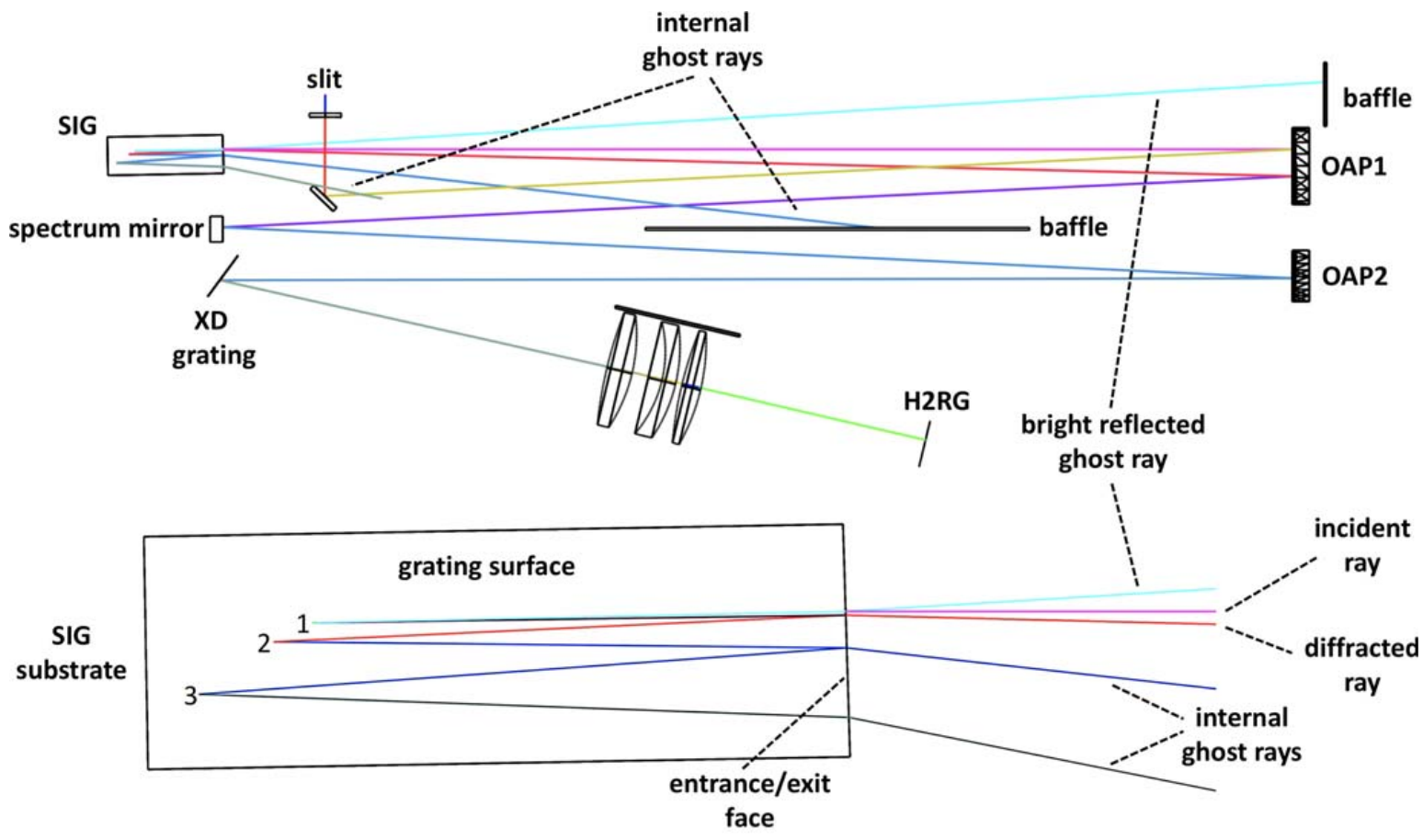


Figure 8. ZEMAX non-sequential single raytrace to identify ghosting in the silicon immersion grating (SIG). The inset view (below) shows detail of the raytrace at the SIG. The grating is tilted with a gamma angle of 1.°025 to direct the diffracted beam towards OAP1 to avoid collision with the incoming beam. The incident ray is partially reflected at the SIG entrance face. The SIG face is wedged 0.°8 to direct this undispersed (bright) reflected ghost away from the diffracted beam and into the baffle just above OAP1. The incident ray is diffracted in immersion by the grating (1). The diffracted ray exits the SIG towards OAP1. On exiting this dispersed (faint) ray is partially reflected and undergoes a second (2) and third (3) diffraction at the grating (relative raytrace cut-off intensity 10^{-6}). These much fainter internal ghosts are also directed away from the primary beam. Only one incident ray is shown for clarity. Millions of rays were traced to optimise the wedge angle and baffle locations. In this view the beam from the slit to the diagonal mirror is folded differently for clarity. The ZEMAX sequential raytrace shown in Figure 4. (Note an earlier version of the camera triplet lens in this raytrace.)

underfilling the array at *JHK*, and optimising for best wavelength cover in the *L*/*L*′ bands (3–4 μm).

The SIG is operated at a temperature of 80 K i.e., about 5 K above the cold bench temperature of 75 K to afford the necessary level of temperature control but not warm enough to result in significant thermal emission. The temperature of the SIG mount is controlled to 80.00 ± 0.02 K (see Figure 7). This minimizes any wavelength shift that would otherwise result due to the change in the refractive index of silicon with temperature (a 0.1 pixel shift for a temperature change of 0.1 K at 2.2 μm, the refractive index is wavelength dependent).

iSHELL was designed under the assumption that there was no useful transmission in silicon below about 1.15 μm (e.g., Marsh et al. 2007). Therefore, one significant surprise during iSHELL commissioning was that the useable transmission of the silicon immersion grating extends down to at least 1.06 μm. However, this is consistent with the work of Macfarlane et al. (1958) that measured the optical absorption edge in silicon at about 1.05 μm at a temperature of 77 K. As a consequence, we added the *J0* mode (see Table 1). Importantly, this gives observers access to the HeI line at 1.083 μm. Unfortunately, instrument throughput is relatively low (<0.05) at wavelengths less than 1.15 μm since the SIG was anti-reflection coated assuming that there was no useful transmission below this wavelength. The low throughput at these short wavelengths (see Table 2) is consistent with the modelled performance of the coating efficiency curve provided by the vendor.

As evidenced by the spectral purity plot (see Figure 9), the groove profile of the delivered SIG ("ES1") is excellent.

4.4. Cross-dispersing Gratings

The cross-dispersing gratings are replica plane-ruled aluminum-coated reflectance gratings from Richardson Gratings[10] (*JHKL*′*M*) and Thor Labs[11] (*L*) used in first order (see Table 1). The fused silica substrates are rectangular, 10 mm thick, 40 mm wide and range in length (depending on blaze angle) from 40 mm to 55 mm. Volume phase holographic (VPH) gratings were not considered for this application due to potential absorption in the grating resins at 3–5 μm.

4.5. Off-axis Parabolic Mirrors (OAPs)

The two off-axis parabolic (OAP) mirrors are single-point diamond-turned (SPDT) from Rapid Solidification Alloy 6061-T6 aluminum so that alignment can be done warm and is not disturbed on cooling. Standard SPDT aluminum has periodic structures (i.e., grooves) in the surface that can be a significant source of optical scatter. To reduce scatter the

[10] https://www.newport.com/b/richardson-gratings
[11] https://www.thorlabs.com

Table 2
Performance of the H2RG Array in the Spectrograph and Some Related Optical Parameters

Parameter	H2RG design	H2RG measured	Note
Format	2048 × 2048		50 pixel border assumed for layout purposes
Wavelength range	1.15–5.3 μm	1.05–5.3 μm	Short wavelength is limited by absorption in Si immersion grating
Slit width	0.″375, 0.″75, 1.″50, 4.″00		3 pixel slit width for 0.″375
Image scale: dispersion direction	0.″125 pixel^{-1}		
Image scale: XD direction	0.″15–0.″21 pixel^{-1}		Anamorphic magnification at XD gratings. Varies with spectral mode
Slit length *J, H, K* *L, Lp, M* *Lp*4	5″ 15″ 25″		
Gain	1.5 e/DN	1.8 e/DN	Varies slightly with individual array gain (Trans-impedance Gain)
Read Noise NDRs = 1 (Non-destructive reads) NDRs = 32	12 e rms 5 e rms	10 e rms (30 ch.) 23 e rms (2 ch.) 4 e rms (30 ch.) 8 e rms (2 ch.)	At 3 μs pixel^{-1} (0.463 s minimum integration time). The array is read out in 32 channels (stripes) each 64 pixels wide. Two channels (ch.) are noisier than average
Dark current + Instrument background	<0.1 e s^{-1}	0.10 e s^{-1} median 0.05 e s^{-1} best area	At 0.312 V bias and after several read outs The best area is an epoxy void region
Full well depth	<50,000 e	71,000 e	At 0.312 V bias
Throughput 1.08 μm	n/a	0.02	A0V star measured through the 4.″0 wide slit in photometric conditions. The BBAR coat on the face of the Silicon immersion grating is not optimized for *J* and shorter wavelengths (see Section 4.3)
1.25 μm	0.08	0.04	
1.65 μm	0.16	0.15	
2.20 μm	0.18	0.18	
3.60 μm	0.17	0.22	
4.80 μm	0.16	0.20	

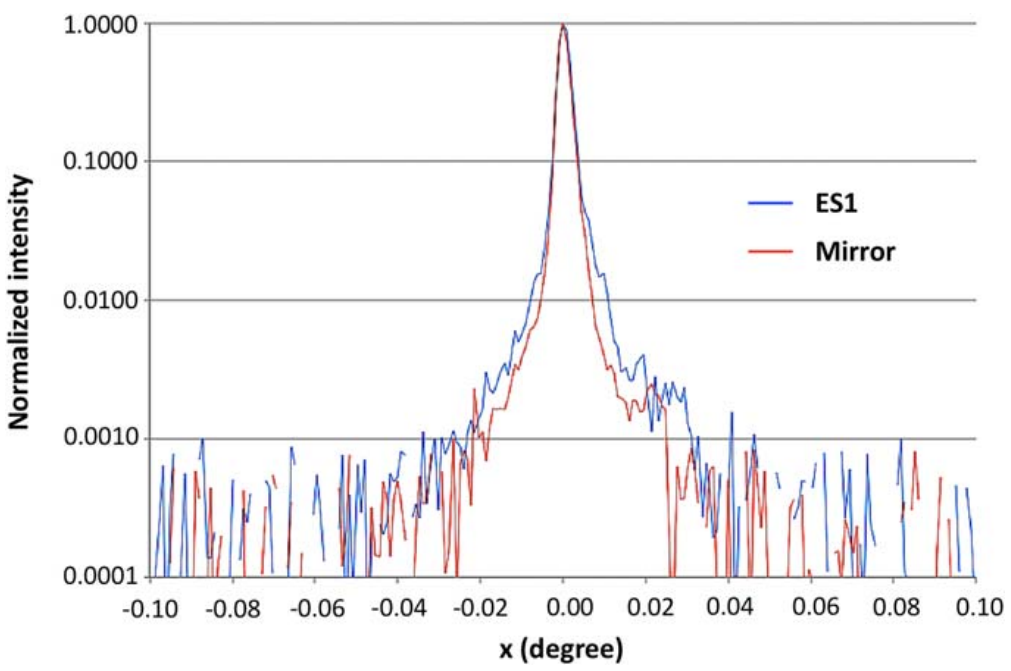


Figure 9. The ES1 grating profile compared with a mirror by reflection at the (un-immersed) back of the grating in the unresolved 0.633 μm He-Ne line. Courtesy of M. Gully-Santiago and C. Brooks, UT Austin.

OAPs are fabricated from Rapid Solidification Process (RSP) aluminum. This is aluminum that is solidified by rapidly cooling from melt forming a very homogenous structure that machines without the "pull outs" that cause the periodic structures. The material is then tempered using the standard T6 process. RSP Technology markets this material.[12] Durham Precision Optics[13] fabricated the OAPs and an integrated aluminum mount, which mounts to the bench by three pads and two pins. One company specializing in machining aluminum mirrors claims that the improved homogeneity is mostly lost once RSP material is cryo-cycled, as it must be for final figuring. However, we see no evidence for this in the performance of our delivered OAPs. OAP1 is 220 mm long, 80 mm wide and 20 mm thick; OAP 2 is 220 mm long, 46 mm wide and 20 mm thick (see Figures 4 and 16).

4.6. Slit Mirrors

The slit mirrors are antireflection-coated CaF_2 substrates with a gold coating (optical depth $>10^3$) and slit aperture applied photo-lithographically to the frontside of the substrate. A metal coating (with uncoated slot) is also applied to the backside to absorb optical ghosts. The slit mirrors are inclined at 22°.5 to the incoming f/38.3 beam to reflect a 42″ diameter field into the slit viewer. A small amount of astigmatism is

[12] http://www.rsp-technology.com/
[13] https://community.dur.ac.uk/cyril.bourgenot/dpo/home/

introduced into the transmitted beam due to the tilt of the substrates. The cryostat window is tilted (to also minimize optical ghosts) in the opposite sense to partially compensate. Since the gold coating is less than one-micron thick, scattering due to the inclined edge of the slit is negligible. The CaF_2 substrates are 30.0 mm diameter and 5.0 mm thick. Max Levy Autograph, Inc.[14] fabricated the slit mirrors. The relatively large thickness is needed to place the internally generated optical ghost onto the absorbing backside metal coating.

4.7. Lenses

The lenses in iSHELL were fabricated and anti-reflection coated by ISP Optics.[15] The three BaF_2-LiF achromatic doublet lenses are relatively standard, all with spherical surfaces and diameters of 40 mm (foreoptics and slit viewer collimator) and 30 mm (slit viewer camera). The simple ZnS pupil-viewer lens mounted in the slit-viewer filter wheel is 19 mm diameter.

Two spectrograph camera lens designs were optimized. All lenses are spherical and about 100 mm diameter. The first was a four-element BaF_2-ZnS-LiF-ZnSe lens. This is completely achromatic across the 1–5 μm, requiring no focusing. However, this design placed the final lens within about 20 mm of the array, allowing little space for an array baffle. The second was a three-element BaF_2-ZnS-LiF lens with the final lens located 102 mm in front of the array, allowing space for an array baffle but requiring ± 1 mm in detector assembly focus to accommodate the 1–5 μm wavelength range of iSHELL.

The addition of an array baffle attached to the array mount, temperature 37 K, significantly reduces the solid angle of the warmer (75 K) enclosure visible to the array. This allows the enclosure to operate at liquid nitrogen temperatures (boiling point 74 K at the altitude of Maunakea) while keeping the photon background from the enclosure well below the level of the array dark current (see Figure 10). We chose the latter scheme since it allowed us to adopt the cooling scheme already in use with SpeX and to use a focus stage design that has operated for 20 yr without incident. Using fewer lenses also improves throughput and reduces stray light.

Since the 95 mm diameter LiF lens is most susceptible to fracture on cooling, it was selected for finite element analysis (FEA). A similarly sized LiF lens in JWST/NIRCam was extensively modelled (Kvamme et al. 2005) and that analysis was used for reference. The three spectrograph camera lenses are mounted in an aluminum barrel. For optical precision each lens is held in place radially by a leaf spring pushing the lens against two fixed radial pads and held in place axially by three coiled springs pushing against three axial pads. The holding force is 2.5 N (250 g) and the lenses become radially centered

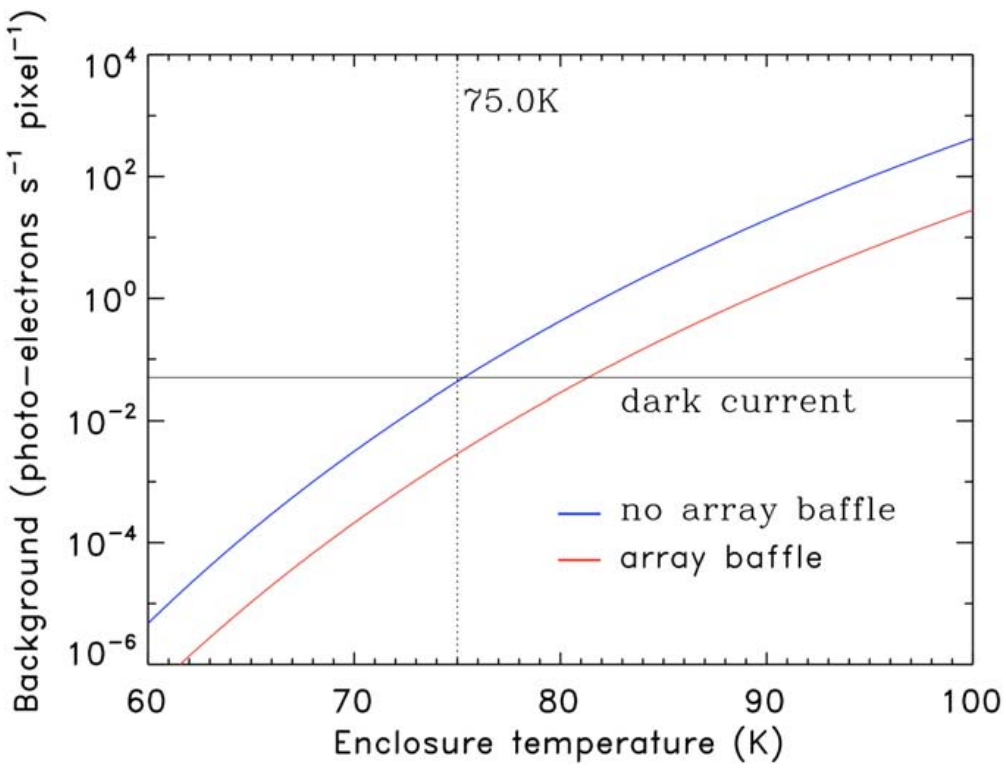


Figure 10. Calculated background signal at a detector pixel plotted as a function of enclosure temperature with i) an array baffle (half-angle 15°) at the temperature of the array (37 K), and ii) without an array baffle (half-angle 90°). The plot assumes a detector cut-off of 5.4 μm and a QE = 1.0. The liquid nitrogen-cooled optical bench and spectrograph enclosure operate at about 75 K.

on cooling. A similar arrangement is used to mount the smaller BaF_2-LiF doublet lenses in the foreoptics and slit viewer.

Analysis of the large LiF lens was done in two parts. A transient thermal FEA was followed by an internal stress FEA. The analysis included the effects of cooling by conduction and radiation, and contact resistance at the mounting points (400 W m^{-2} K^{-1}). We found that a cooling rate of less than 0.5 K min^{-2} was required to the keep the stress in the lens (1.25 Mpa) well below that recommended by the NIRCam analysis (maximum resolved stress 2.0 Mpa). This is done by thermally isolating the aluminum lens barrel from the liquid nitrogen-cooled optical bench by fiber-glass washers. The assembly mounts to the bench by three pads and two pins for registration.

4.8. Th-Ar Lamp

In the original design of the calibration system a low-pressure Th-Ar lamp was fed into a custom-made integrating sphere from Labsphere.[16] However, the arc lines proved to be much too faint to be useful due to light losses in the integrating sphere. This was fixed by moving the lamp into a position where it could be moved directly over the entrance window during calibration (see Figure 2). Inevitably, without the spatial scrambling properties of the integrating sphere, the arc line illumination at the slit is no longer perfectly flat and arc line profiles along the slit are slightly variable, requiring mitigating measures in the spectral extraction software.

[14] https://www.maxlevy.com/
[15] https://ispoptics.com/
[16] https://www.labsphere.com/

Due to International Traffic in Arms Regulations (ITAR) restrictions no commercial companies currently make Th-Ar lamps with the pure ^{232}Th cathodes formerly employed, because of the radioactive properties. The Photron[17] lamp in iSHELL uses a ThO_2 cathode, which leads to spectral contamination (see Figure 3) and complicates arc line identification (e.g., Nave et al. 2018). The rich spectrum of arc lines from the low-pressure Th-Ar lamp are unresolved at $R = 80{,}000$ (line widths $<4\,\mathrm{km\,s^{-1}}$) compared to the sparse lines from a high-pressure Ar lamp (line widths $>8\,\mathrm{km\,s^{-1}}$). Compared to the 1–2.5 μm range far fewer Th-Ar lines are available for wavelength calibration over the 3–5 μm range due to the increasing opacity of the lamp's quartz envelope and the resulting thermal emission from the envelope. For wavelength calibration at 3–5 μm and we make extensive use of the rich telluric spectrum that comes for "free" during observing.

5. Cryostat Design, Fabrication and Assembly

5.1. Cooling

The cryostat is of similar size to SpeX (about 0.5^3) and uses the same conservative cooling design. It contains a bench to which the optics are mounted. A liquid nitrogen can that is mounted to the bench cools it and the surrounding light-tight enclosure to about 75 K. This is required to keep the thermal background from the enclosure below the detector dark current (see Figure 10). The radiation load onto this cold structure is minimized by surrounding it with a radiation shield, which is cooled by attaching it to the first stage of a CTI-Cryodyne 1050 CP closed-cycle cooler to about 115 K. The spectrograph and slit viewer arrays are cooled to 37 K and 30 K respectively, using the second stage of the cooler, and controlled to ± 0.01 K. LakeShore[18] 335 temperature controllers provide temperature control of the arrays and SIG. Cooling to operational temperature takes about three days (see Figure 11).

5.2. Fabrication

Except where noted all machining was done in-house at the Institute for Astronomy, Honolulu. Atlas Technologies[19] fabricated the vacuum jacket. It is a four-sided TIG-welded Al 5056-T0 structure with two Al 6061-T6 covers. Al 5056-T0 is used for the main structure since it retains its strength and does not require heat-treating after welding. For optimum vacuum integrity the parts were milled from billets. All the service ports for wiring and cooling are machined into the center section. Removing one cover gives access to the foreoptics side while removing the other cover gives access to the spectrograph side. The O-ring grooves are machined into the covers with a dovetail shape to prevent the O-rings from falling out during assembly and maintenance. The inside of the vacuum jacket is highly polished for low emissivity (see Figure 12). No multi-layer thermal insulation is needed. The external dimensions of the vacuum jacket are $1.31 \times 0.70 \times 0.70$ m. A telescope interface box is welded to the top plate of the vacuum jacket. This box contains the calibration unit (see Figure 2). The total weight of the vacuum jacket including the interface to the telescope is 265 kg.

The spectrograph and foreoptics (including the slit viewer) are mounted on opposite sides of the optical bench, which is milled from a single ingot of aluminum 6061-T6. For positional precision, final machining followed cryogenic cycling of the bench. In addition to pocketing and drilling access holes for optical and mechanism mounts, the bench contains covered channels for mechanism wiring to shield the detectors from

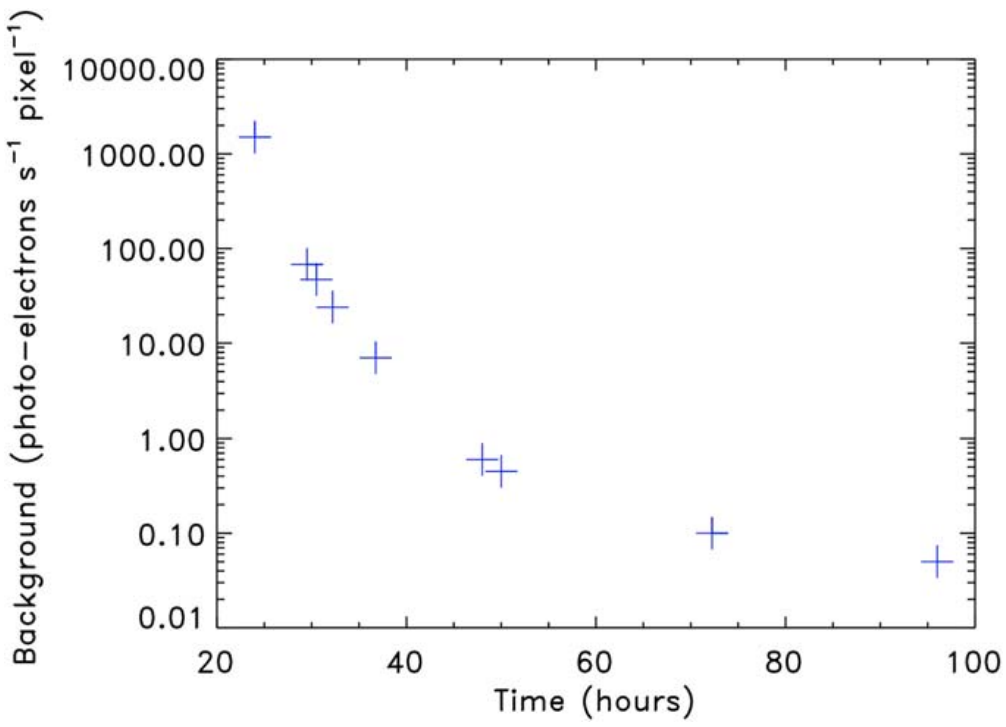


Figure 11. Measured spectrograph background signal, including dark current, during cooling. The signal bottoms out at about 0.05 e s^{-1} after about four days of cooling (see Section 8).



Figure 12. The interior of the Al 5056-T0cryostat vacuum jacket is highly polished to minimize heat load on the cold structure.

[17] https://www.photronlamp.com/
[18] https://www.lakeshore.com/
[19] https://www.atlasuhv.com/

potential thermal emission from warm wires entering the cryostat. Two light-tight (except for the optical beam entry port) aluminum covers enclose the optical bench. The covers are needed to shield the detectors from photons emitted by the warm vacuum jacket. They attach to the optical bench by a bolted tongue-and-groove interface to minimize light leaks. (An unfiltered 5.4 μm cutoff detector detects 10^4 times as many thermal photons from an object at room temperature as an unfiltered 2.5 μm cutoff detector). The light-tightness of the covers was checked by placing bright flashlights inside the sealed enclosure and by using intensified goggles to search for light leaks, with the enclosure inside a darkroom. The covers are highly polished on the outside for low emissivity and painted black (Aeroglaze Z306) on the inside to absorb scattered light. Cardic Machine Products,[20] Inc., fabricated the optical bench and enclosure covers.

For cooling a 12-l capacity liquid nitrogen can (540 W-hr), also made by Atlas Technologies, is bolted directly to the optical bench. The can is machined from an Al 6061-T0 billet with a TIG-welded cover added. Two stainless steel fill tubes connect the can to the fill ports in the vacuum jacket. Each tube has a Swagelok bellows at the top and bottom for mechanical compliance on cooling. The fill tube assembly attaches to the liquid nitrogen can via an indium-wire sealed flange plate. Four V-shaped titanium trusses attach the optical bench to the vacuum jacket. Titanium is used for stiffness, thermal isolation and ease of assembly. The weight of the optical bench including the covers and liquid nitrogen can is 102 kg, and 202 kg with the mechanisms and optics added.

The radiation shield reduces the thermal load on the optical bench. It is made from six 3 mm thick Al 6061-T6 plates bolted together, weighs 31 kg, and was fabricated by Bear Machinery, Inc.[21] The plates are highly polished for low emissivity. For mechanical support and thermal isolation several G-10 mounting tabs attach the radiation shield to the vacuum jacket. The side covers of the radiation shield corresponding to the side covers of the vacuum jacket contain no feed-throughs and are removable to give access to the foreoptics and spectrograph.

We estimate the emissivity of the highly polished aluminum surfaces—the inside of the vacuum jacket, the actively cooled radiation shield, the outside of the cold bench enclosure covers and the liquid nitrogen can, to be about 0.05. The total heat load on the liquid nitrogen can is estimated to be about 10 W (conduction through the titanium mounting trusses 5.0 W, conduction through cold motor wiring 3.0 W, window radiation 0.8 W, radiation from the actively cooled radiation shield 0.5 W, and SIG temperature control 0.3 W), which is consistent with the measured liquid nitrogen hold-time of about two days with the telescope parked at zenith.

[20] https://www.cardicmachine.com/
[21] https://www.bearmachineryinc.com/

The total weight of the cryostat including all the optical components, mechanisms, and cryostat-mounted electronics boxes is 520 kg.

5.3. Mechanisms

iSHELL contains eight cold mechanisms (see Figure 2). The slit wheel, order-sorter filter wheel and slit-viewer filter wheel are detented Geneva mechanisms. When in position the wheels are immobile and decoupled from the drive. The wheel position is accurately defined by the detent and not by the drive train. The detent is lowered into position with a cam attached to the drive. The k-mirror image rotator requires continuous rotation to reach any position angle on the sky, and employs a worm gear. To remove backlash, the worm is radially preloaded against the worm gear with a wire-EDM fabricated parallel flexure stage. The spectrograph detector focus stage employs a planetary gear for gear reduction and a lead screw for translation (a few mm of focus is required). The array mount is itself mounted on a parallel flexure stage, which only allows movement in the focus direction. To remove backlash, a preloaded split nut is used for the lead screw. In the Dekker mechanism a mask with three sections defining the slit lengths is mounted on a stage attached with two parallel linkages that have flex pivots at both ends. A crankshaft and worm gear train drive the stage in a slightly arced motion. The arced motion is compensated for by the location of the individual slit masks.

The cross-disperser grating turret contains two mechanisms: a detented eight-position grating wheel, and a tilt mechanism to tilt the entire wheel $\pm 5^\circ$ about the optical axis parallel to the grating grooves through the center of the grating. A tilt mechanism is required to move spectral orders up and down on the array (see Table 1 and Figure 3). The turret is rotated by a pre-loaded worm gear and is held accurately in position by an arm with a bearing at its end that rolls and drops into V-shaped detents. On the rotation axis a flexure-bearing mount stays aligned when warm and compensates for contraction on cooling. In the tilt mechanism two large flex pivots are mounted along the optical axis on each side of the turret (see Figure 13) and a preloaded lead nut assembly pushes the turret around the tilt axis. The moving weight of the grating turret is 5 kg with a wheel diameter of about 150 mm. The mechanism was specified for one-pixel reproducibility in the cross-dispersion (a precision of 30″ due to the long lever arm) and although this stability was achieved the reproducibility was only within about ten pixels. The spectral extraction software is able to accommodate this uncertainty.

All the cold mechanisms are driven with cryogenically qualified VSS-43 Phytron[22] motors except the Dekker mechanism, which uses a smaller VSS-25 Phytron motor. All the metal gears in the mechanisms were coated with molybdenum

[22] https://www.phytron.eu/

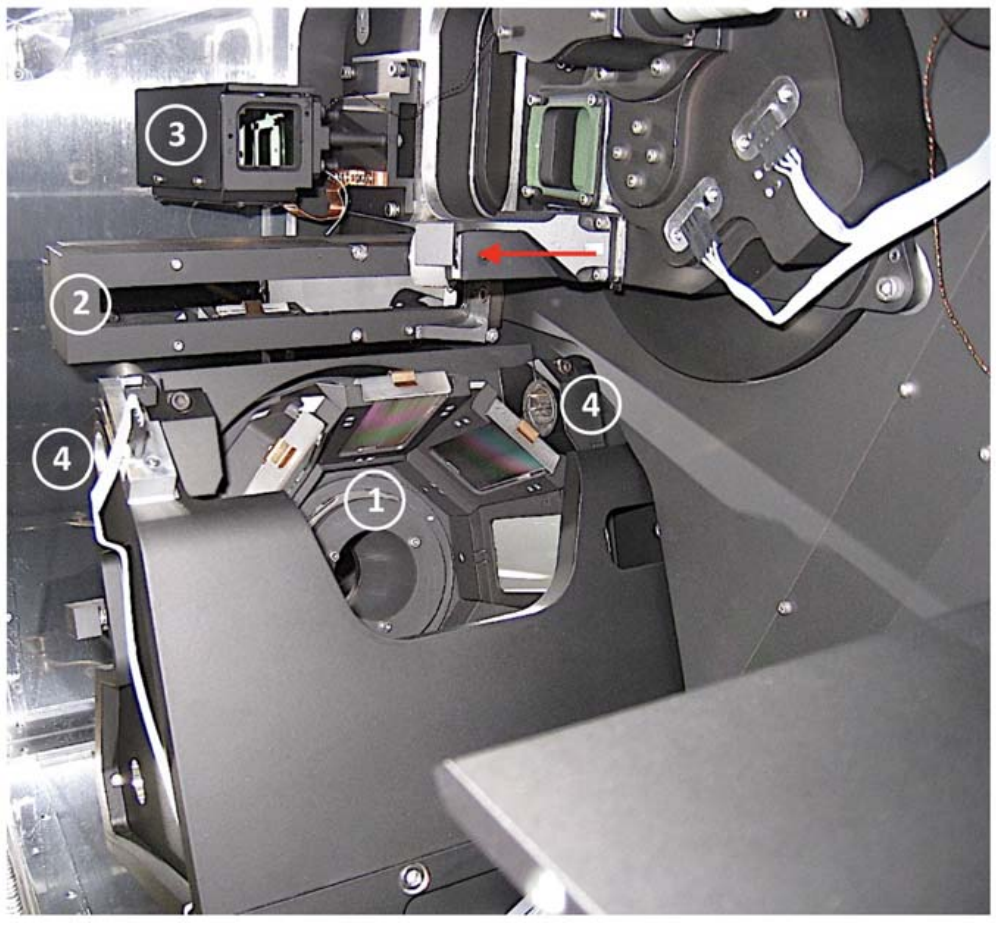


Figure 13. A view of the cross-disperser grating turret (1) with the spectrum mirror (2) and immersion grating (3) above it. The grating tilt flex pivots are also visible (4). The red arrow indicates the direction of the beam entering the spectrograph before a 90° reflection at the small mirror towards the OAPs located to the right of this figure (see Figure 16).

disulphide (MoS_2) using a vacuum sputtering process. For the worm gear trains in the image rotator and cross disperser, the worms were fabricated from Vespel SP-3, which is a Polyimide plastic coated with MoS_2. All the ball bearings in the mechanisms were dry lubricated with MoS_2 using a spray and bake process. The four warm mechanisms on top of the vacuum jacket are all driven by precision Micronix linear stages.[23] Mechanism position sensing is done with non-contact Hall Effect sensors and magnets.

5.4. Assembly and Alignment

The assembly procedure of iSHELL is illustrated in Figure 14. This was done in the clean room in the IRTF Lab, Honolulu. The optical bench was lowered into the vacuum jacket using a gantry crane. Once the performance of the cryostat was qualified the mechanisms were installed and tested. Preliminary warm testing of the mechanisms was done with warm-use only Phytron motors. Only limited testing was possible with the cryogenically qualified Phytron motors (energized for less than one minute) in order to complete functional checks. The optics were installed once the cold mechanisms were working properly.

Initial alignment was done with an optical alignment telescope mounted on the cryostat vacuum jacket at the window and with alignment targets in the optical mounts, and shimming the mounts, in sequence, down the optical chain as necessary. This was done without the k-mirror image rotator in place.

Due to the 27° of freedom (three mirrors each with three axes) it is very difficult to precisely align the mechanical axis of the k-mirror with the optical axis. Therefore, the k-mirror was built as one machined assembly with tight specifications. Importantly, since it is located close to the cold stop (the pupil) in the foreoptics any misalignment does not move the reimaged pupil on the immersion grating in the spectrograph. Any misalignment at the slit (the reimaged telescope focal plane) when the position angle is changed is corrected by simply repointing the telescope. (Since IRTF is an equatorial telescope only one repointing is required for a given position angle). The specification was for a misalignment on any rotation of less than 10% of the 42″ FOV of the slit viewer and this was met.

Next the proxy mirror for the SIG was replaced with the SIG. Since silicon is opaque in the visible the initial alignment of the immersion grating was done by tilting the SIG to place the visible reflection off the wedged front face of the SIG at the location on the baffle above OAP1 (see Figure 2) modelled in ZEMAX. The front face is wedged by 0.°8 to avoid sending the undispersed ghost reflection towards the detector. Final alignment of the SIG was done during all-up cold tests. This required measuring the location of the peak of the blaze function on the array and, following warm up, re-machining the base of the immersion grating mount by the calculated amount to place the peak of the blaze in the central column of the array. A similar procedure was required to align the long axis of the slits on the spectrum mirror by adjusting the base in the direction normal to the blaze correction. The final alignment of the SIG required two cooldowns.

Figures 15 shows the fully assembled foreoptics (including the slit viewer). Note the long baffle tubes to minimize off-axis flux entering the foreoptics at the entrance window and the added sub-plate over the slit area to minimize stray light entering the spectrograph. Figure 16 shows the fully assembled spectrograph.

Optical alignment of the instrument cold stop to the entrance pupil (the telescope secondary mirror) was done by viewing the image of the secondary mirror conjugated onto the cold stop using the pupil viewer optics in the slit viewer and by shimming the instrument mount to the telescope (see Figure 17).

6. Array and Instrument Control

iSHELL uses a 2048×2048 H2RG array in the spectrograph and a 512×512 Aladdin 2 InSb array in the slit viewer. A fundamental requirement of the slit viewer is that the read out must operate independently of the spectrograph read out, i.e., with the exception of moving mechanisms and slewing the telescope, there must be no mutual influence on the operation of the two arrays

[23] https://micronixusa.com/

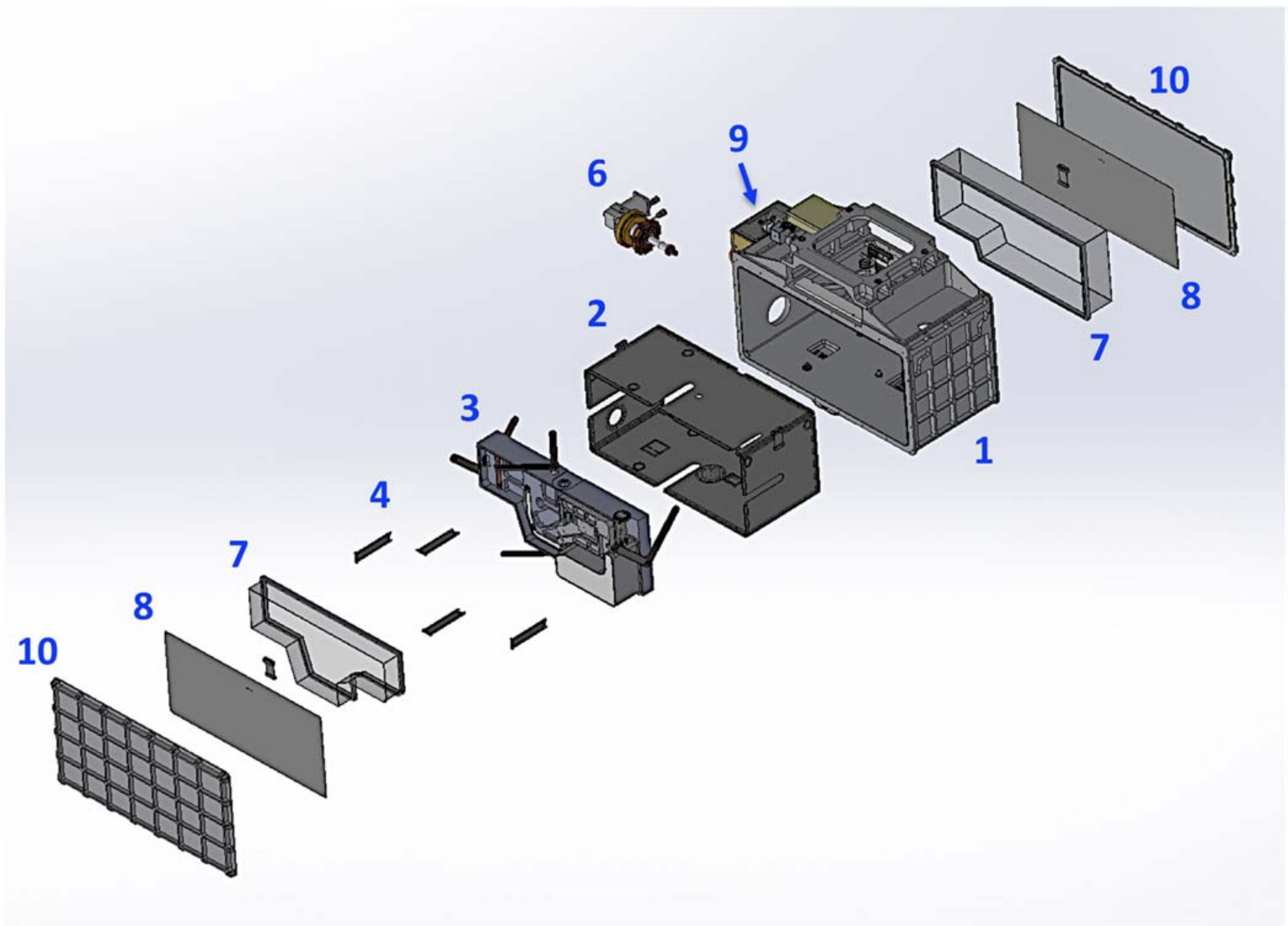


Figure 14. Stages in the assembly of iSHELL: (1) The center section of the cryostat vacuum jacket. (2) Install the radiation shield into the vacuum jacket. (3) Install the optical bench with trusses attached. (4) Install the truss covers into the radiation shield. (5) Install wire harnesses (not shown). (6) Install the 1050 CP cryo-cooler and thermal straps. (7) Install the light-tight optical bench covers. (8) Install the radiation shield covers. (9) Install the array controllers. (1)0 Install the cryostat covers. Mechanisms, optics and detector arrays are installed following satisfactory testing of the cryostat.

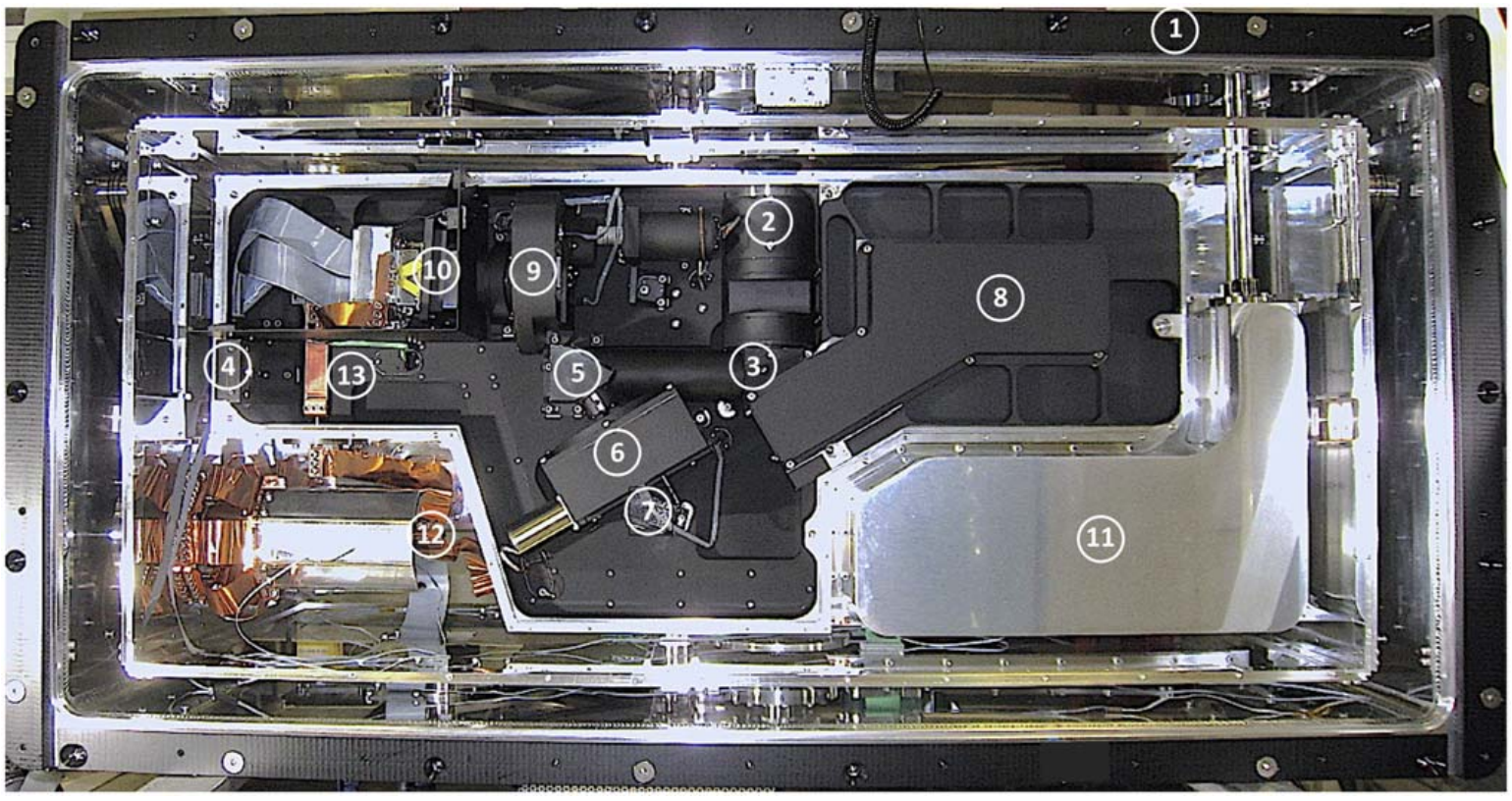


Figure 15. The fully assembled foreoptics on the optical bench with the covers removed. The three nested rectangular structures are, from outside in, the vacuum jacket, radiation shield, and optical bench. The black Delrin strips (1) are installed to protect the vacuum jacket O-ring surface once its cover is removed. Optical components in order along the light path are the entrance window and baffle tube (2), fold mirror (3), collimator mirror (4), fold mirror (5), k-mirror image rotator (6), fold mirror (7), slit mechanism (8, covered), filter wheel (9) and slit-viewer array mount (1)0. Other components include the liquid nitrogen can (11), the closed-cycle cooler (12), and the copper foil thermal path (1)3 connecting the second stage of the cooler to the slit-viewer array mount. See Figure 2 for the unfolded schematic layout.

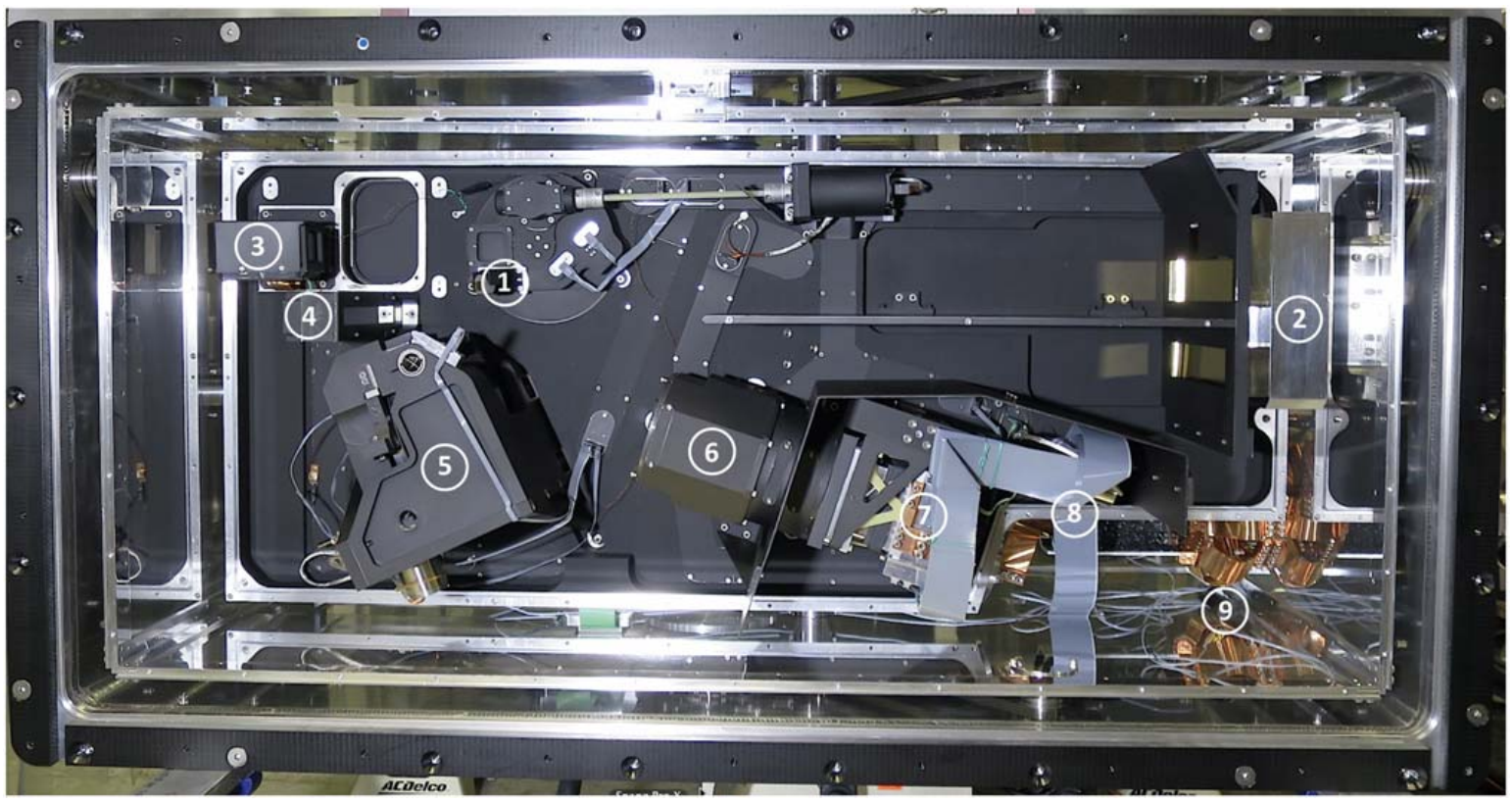


Figure 16. The fully assembled spectrograph on the optical bench, with the covers removed. The three nested rectangular structures are, from outside in, the vacuum jacket, radiation shield, and optical bench. Light enters the spectrograph through the order-sorter filter wheel (1). Optical components include in order along the light path the off-axis parabolas (2), the silicon immersion grating (3), spectrum mirror (4), cross-dispersing grating turret (5), camera triplet lens (6), and the H2RG array mount (7). See Figure 2 for the schematic layout and Figure 4 for the ZEMAX raytrace. Other components include the ribbon cabling connecting the external array controller to the spectrograph array (8), and the copper foil "crown" connecting the radiation shield to the first stage of the closed-cycle cooler (9).

(independent computer operation, independent data transfer and storage, no need to sequence integration times or read outs, no induced noise or electrical pickup). This required careful electrical grounding. Astronomical Research Cameras (ARC), Inc.,[24] Generation 3 controllers are used for both arrays. The controllers are identical to those used in SpeX following its upgrade in 2014. SpeX uses the same arrays. We chose the ARC controllers over other electronics, such as the Teledyne Sidecar ASIC for several reasons. The ARC controllers meet and exceed the performance requirements and IRTF staff have prior experience with the ARC electronics for H2RGs and other devices. They are also backward and sideways compatible between SpeX and iSHELL and are easy to maintain.

The H2RG array controller electronics require a 12-slot housing (dimensions $33 \times 16 \times 27$ cm) containing: one ARC-22 fiber optic timing board, one ARC-32 IR and CCD clock driver board, and four 8-channel IR video boards (16 bit A/Ds, pre-amps, and biases). Four video boards are needed to read out the 32 channels of the H2RG plus a fifth board for reading out bias voltages (primarily for engineering diagnostics). We also needed to add a custom board for more stable bias voltage supply. For operational reasons the H2RG is wired for 32 outputs since we require the device to be interchangeable with the array in SpeX, which requires integration times as short as 0.463 s (3 μs per pixel).

The smaller InSb array controller electronics use a 6-slot housing (dimensions $33 \times 16 \times 14$ cm) containing: one ARC-22 fiber optic timing board, one ARC-32 IR and CCD clock driver board, and one 8-channel IR video board (16 bit A/Ds, pre-amps, and biases). Power for each controller is provided by two Agilent[25] N6700B supplies. Manganin ribbon cabling is used for internal array wiring as in SpeX.

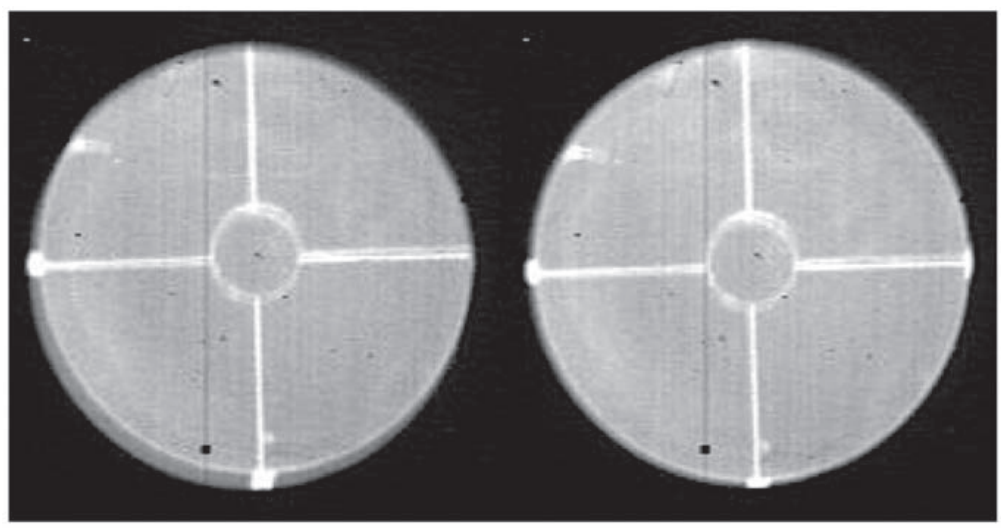


Figure 17. Telescope secondary mirror and foreoptics cold stop imaged at 3.5 μm with the pupil viewer, before (left) and after (right) shimming the instrument mount to the telescope (a 0.6 mm shim for about 10 mm movement at the 244 mm diameter secondary mirror). The secondary mirror image, which shows the edge of the primary mirror (left), is conjugated with the cold stop in the foreoptics.

The two array controller boxes are mounted to the outside of the cryostat vacuum jacket, close to the arrays they control, to minimize analog wire lengths. Each of the array controllers is controlled by its own PC, which is located in the telescope control room. The PCs currently run CentOS Linux. A 100 m long receive and transmit fiber runs between each controller mounted to the instrument and a PCIe board in each PC in the telescope control room. A third instrument control PC is

[24] https://www.astro-cam.com

[25] https://www.agilent.com

responsible for all other aspects of instrument control (mechanisms, temperature, housekeeping etc).. Two Lakeshore LM335 Cryogenic Temperature Controllers provide temperature control of the two arrays and the SIG. All three PCs are on the IRTF local area network. Ancillary equipment for instrument control that needs to be close to the cryostat (e.g., motor drivers, temperature controllers, power supplies etc). is housed in cooled instrumentation boxes that attach to the primary mirror cell ("coolracks").

Observers interface with iSHELL via Graphical User Interfaces (GUIs) that run on the spectrograph and slit viewer PCs in the same way that observers currently use SpeX. The GUIs can be operated remotely via VNC. About ninety percent of IRTF observers work remotely, from their home institutions or homes.

7. Data Reduction

Given the cross-dispersed nature of the spectra and the similarity of the data structure and format to those generated by SpeX, we decided to base the data reduction system for iSHELL on the IDL-based Spextool package (Cushing et al. 2004). Important modifications to the code include updating the GUIs to accommodate the large number of orders covered by iSHELL (up to about 30) compared to SpeX (up to six) and dealing with the tilted slits in iSHELL (see Section 4.3). As a result of the tilt a given wavelength spans many detector columns. This requires: (1) generating a one-dimensional wavelength calibration appropriate for the middle of the slit in each order, in the same manner as used for SpeX data; (2) generating a distortion map; (3) rectifying the data onto a regular grid such that wavelength is at a fixed column in each order.

The flux calibration and telluric correction routine developed by Vacca et al. (2003) is used with only minor modifications for iSHELL data. The procedures require separate observation of an A0 V telluric standard star, which ideally should be at least as bright, if not substantially brighter, than the science target. This can be problematic since a nearby (i.e., similar airmass) A0V standard star is not always available. However, we have made progress on using atmospheric modelling of iSHELL data to remove telluric features without the need for taking a telluric standard star[20].

At 1–2.5 μm wavelength calibration uses the Th-Ar lamp. However, compared to the 1–2.5 μm range, far fewer Th-Ar lines are available for wavelength calibration at 2.9–5.3 μm due to the increasing opacity of the lamp's quartz envelope and the resulting thermal emission from the envelope. For wavelength calibration over this range we make extensive use of the rich telluric spectrum that comes for free from the science data and that does not require separate wavelength calibration. An atlas of Th-Ar lines and telluric features used for wavelength calibration of iSHELL is available online at the IRTF website,[26] where Spextool is also available for download.

[26] http://irtfweb.ifa.hawaii.edu/research/dr_resources/

8. Performance

With few exceptions (see Section 10) iSHELL has met all design specifications. Table 2 lists performance parameters of the H2RG array in the spectrograph and some related optical specifications. The full array read out time of 0.463 s is the time required for one non-destructive read (NDR). To reduce read noise, multiple NDRs sample signal by reading up the signal ramp (known as Fowler sampling, see Fowler & Gatley 1990 and Figure 1 in Vacca et al. 2004). Each NDR is a correlated double sample. By default, the array does as many NDRs as possible up to a maximum of 32 (on-chip integration time 14.8 s and longer), beyond which there is little improvement in the read noise. The measured well depth is 71,000 photoelectrons (0.312 V bias). However, recommended integrations times are limited to keep the integrated signal below half-full well. This keeps the signal in the range that can be corrected for linearity to better than about 1%. Correction for linearity is part of the Spextool data reduction procedure (Vacca et al. 2004).

We see minimal evidence of residual image (<1% of previously exposed signal) or persistence (<10% of dark current) in our H2RG array. The measured median dark signal (dark current plus any background light leak) stabilizes after several 600 s integrations at 0.10 e s^{-1} and at 0.05 e s^{-1} in a small "epoxy void" region (3% of the array). Epoxy should completely fill the layer between the multiplexer and detector substrates. In an analysis of a JWST 5 μm cutoff H2RG device, Regan & Bergeron (2020) conclude that the apparent "dark current" is due to multiplexer glow and that it is not generated in the HgCdTe detector material at temperatures lower than 60 K. They also see low signal in an epoxy void region and hypothesize that the epoxy channels multiplexer glow into the detector material due to a better refractive index match than in the void.

The measured spectral line spread functions and resolving powers in the *J2*, *H2*, *K2* and *L1* modes (see Table 1) and the narrow slit (0.″375) are shown in Figure 18. The best fit profiles are Voight profiles. Measurements are made by stacking up about 30 individual Th-Ar lines in each of the modes to improve S/N. The measured resolving powers at the center of the free spectral range (FSR) are listed in Table 3. The higher resolving power in the *M1* and *M2* modes is most likely due to the effects of diffraction (see Section 4.2 and Figure 5). The higher resolving power at *M* is also consistent with that measured on unresolved CO absorption lines observed towards Herbig Ae/Be stars (about $R = 92{,}000$, Banzatti et al. 2022).

Similarly, the measured resolving powers at the center of the free spectral range (FSR) for the 0.″75 slit are also listed in Table 3. In the latter case the errors are smaller since the Th-Ar lines are better sampled. Note that all the Th-Ar line measurements are made with the slits evenly illuminated. Higher resolving powers can result if a point source, for

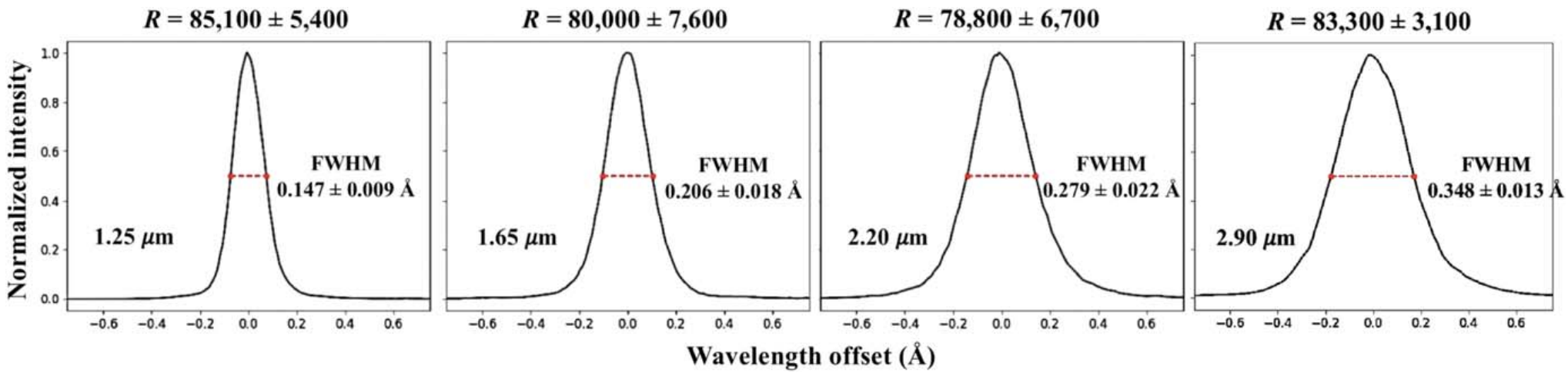


Figure 18. Spectral line spread functions and the resolving power of iSHELL measured from Th-Ar lines and the 0.″375 slit in the *J2* (1.25 μm), *H2* (1.65 μm), K *3* ((2.20 μm), and *L1* (2.90 μm) modes (see Table 1). About 30-40 individual lines are stacked to improve the S/N. The best fit is a Voight profile. The errors shown are the standard deviations of the profile fits. In these measurements the arc line illumination evenly fills the slit (see Section 4.8).

example, underfills the slit, in particular for slit widths 0.″75 and wider.

Table 4 lists performance parameters of the engineering grade Raytheon 512×512 Aladdin 2 InSb array in the slit viewer. The slit viewer is used for object acquisition and guiding. It is equipped with eight filters covering 1–5 μm. This array was fabricated in 1998 for the SpeX project. It comes from the edge of the die used to fabricate the original 1024 × 1024 InSb array (since upgraded with a H2RG). Despite the higher than nominal read noise and dark current, imaging with the slit viewer is source or sky background limited for most acquisition and guiding needs.

Table 3
Measured resolving power (R) at center of FSR

Mode	Slit width	R
J2	0.″375	85,100 ± 900
H2	0.″375	80,000 ± 1300
K2	0.″375	78,100 ± 1100
L1	0.″375	83,300 ± 500
M1/M2	0.″375	88,100 ± 2000
J2	0.″75	48,200 ± 300
H2	0.″75	50,800 ± 400
K2	0.″75	47,600 ± 400
L1	0.″75	49,800 ± 400
M1/M2	0.″75	53,300 ± 300

Note. The errors given are the standard error on the mean.

9. Observing with iSHELL

9.1. Using iSHELL

The workhorse $R = 50$-2500 infrared spectrograph and imager, SpeX, currently averages about 55% of allocated observing time on IRTF. Being more specialized, iSHELL science programs average about 30% of allocated observing time. Table 5 gives a breakdown of the iSHELL science programs by scientific category over the past several semesters and roughly align with the expectations of the science case. Of these programs about 60% are primarily 2.7–5.3 μm programs and about 40% primarily 1–2.5 μm programs.

In the *J*, *H* and *K* observing modes (see Table 1) the slit length of 5″ is too short for nodding point sources. However, at iSHELL resolving powers the sky background is negligible compared to the dark current (see Figure 1) except on the sparse sky emission lines, which can be fitted along the slit. Instead, a dark exposure of the same integration time is subtracted from the target exposure made in the center of the slit. In the *L*, *Lp* and *M* observing modes (see Table 1) the slit length of 15″ allows point sources to be nodded within the slit so that the brighter and more variable sky background can be subtracted without any loss of efficiency. Extended sources are nodded out of the slit if a sky exposure needs to be subtracted.

The internal k-mirror image rotator (see Figure 2) is used to align the slit with the required position angle on the sky. Due to the smaller one-shot wavelength range of iSHELL compared to medium resolution spectrograph, SpeX, there is no need to set the position angle to the parallactic angle for point sources. In both iSHELL and SpeX, the image rotator remains stationary during integrations.

Wavelength calibration and flat fielding are done using standard macros (scripts). The macros move mechanisms, turn lamps on and off in the calibration box, but do not move anything inside iSHELL. The macros return the instrument to the configuration in which the macro is started; no observer intervention is required. Due to flexure and mechanism reproducibility the calibration macros must be executed immediately before or after changing observing mode. Observing procedures are detailed in the online instrument manual.[27]

9.2. Example Observing Programs

During commissioning of the *J0* mode we observed the bright luminous blue variable (magnitude $J = 6.1$) MWC 314 with the 0.″375 slit ($R = 85{,}100$, see Figure 18 and Table 3). A

[27] irtfweb.ifa.hawaii.edu/~ishell/observer

Table 4
Performance the Aladdin 2 InSb Array in the Slit Viewer and Some Related Optical Parameters

Parameter	iSHELL	Note
Format	512×512	
Wavelength range	0.9–5.5 m	
FOV	$42''$ diameter	Field of view underfills the array by design
Sub–array read out	Yes	
Image scale	$0\farcs1040 \pm 0\farcs007$ pixel^{-1}	
Gain	17 e/DN	
Read Noise NDRs = 1 NDRs = 16	110 e rms 45 e rms	At 7 μs pixel^{-1} (0.241 s minimum integration time)
Dark current + instrument background	10 e s^{-1}	At 0.400 V bias when stable
Well depth	90,000 e	At 0.400 V bias (the default)
	~120,000 e	At 0.700 V bias (useful for nbM imaging)
Throughput	*J*	0.17 From standard star measurements
	K	0.33

Table 5
iSHELL Observing Scientific Category 2019–2020

Observing program	Allocation
Planetary atmospheres	18%
Comets	10%
Exoplanet radial velocity	7%
Exoplanet characterization	10%
Debris disks	7%
Protoplanetary disks	17%
YSOs	8%
Stellar astrophysics	12%
Interstellar medium	10%
Extragalactic	1%

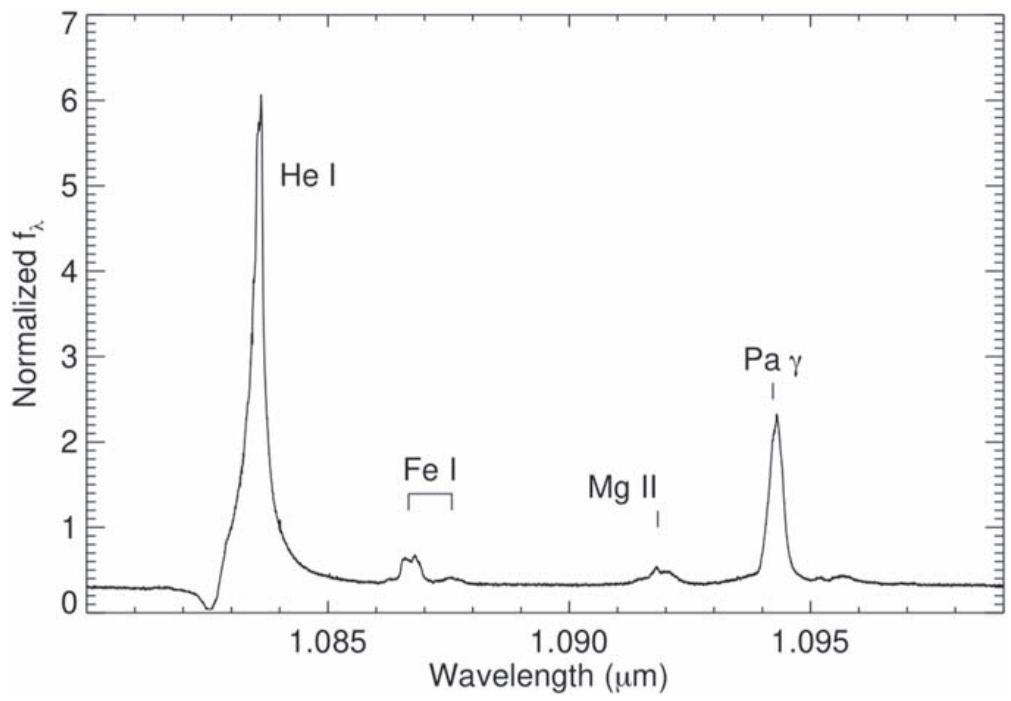


Figure 19. A subset of the *J0* mode spectrum of the LBV MWC 314 taken with the $0\farcs375$ slit ($R = 85{,}100$). The integration time is 540 s and the S/N on the continuum is 150, smoothed over the slit width. The instrument throughput is relatively low in this mode (see Section 4.3 and Table 2). The emission line identifications are from Groh et al. (2007) shifted to the radial velocity of the source (+29 km s^{-1}).

subset of the spectrum is plotted in Figure 19. Most prominent is the He I 1.0830 μm emission line formed in the outflowing stellar wind together with a high velocity P Cygni absorption wing (Groh et al. 2007).

Flores et al. (2020) are using iSHELL for observations of YSOs in the *H* and *K* modes to measure temperature, surface gravity, magnetic field strength, and rotational velocity. This is done by fitting synthetic stellar spectra to the high-resolution spectra (see Figure 20). The accuracy of the method is checked by also fitting the synthetic spectra to a sample of main sequence stars.

iSHELL is not a precision RV-optimized infrared spectrograph. It is mounted at Cassegrain focus and optics are moved to change observing modes, and so it is not optimized for stability. Also, IRTF scheduling is not well-suited for multi-epoch RV observing programs. Nevertheless, through the use of the methane gas cell provided by Peter Plavchan's group, now at the George Mason University, iSHELL is proving productive for some RV studies of young stars. RV observations are made with the gas cell inserted into the beam (see Figure 2), imprinting wavelength calibrated absorption lines onto stellar spectra.

A good example are the observations of AU Mic. AU Mic is a pre-main sequence star with a spatially resolved edge-on debris disk. iSHELL RV observations by Plavchan et al. (2020) have helped confirm the presence of the transiting planet AU Mic b (see Figure 21). Observations of a planet co-existing with a debris disk offer the opportunity to test the predictions of current models of planet formation and evolution.

By observing AU Mic b in transit, Martioli et al. (2020) combined SPIRou (Donati et al. 2020) and iSHELL RV observations to measure the Rossiter-McLaughlin effect (see Figure 22). The analysis shows that the orbit of AU Mic b is prograde and aligned with the stellar rotation axis with a sky-projected spin–orbit obliquity of $0^{\circ}_{-15^{\circ}}{}^{+18^{\circ}}$. The aligned orbit of AU Mic b indicates that it formed in the protoplanetary disk that evolved into the current debris disk around AU Mic. Martioli et al. (2020) conclude that the agreement between the data sets from these two different instruments using

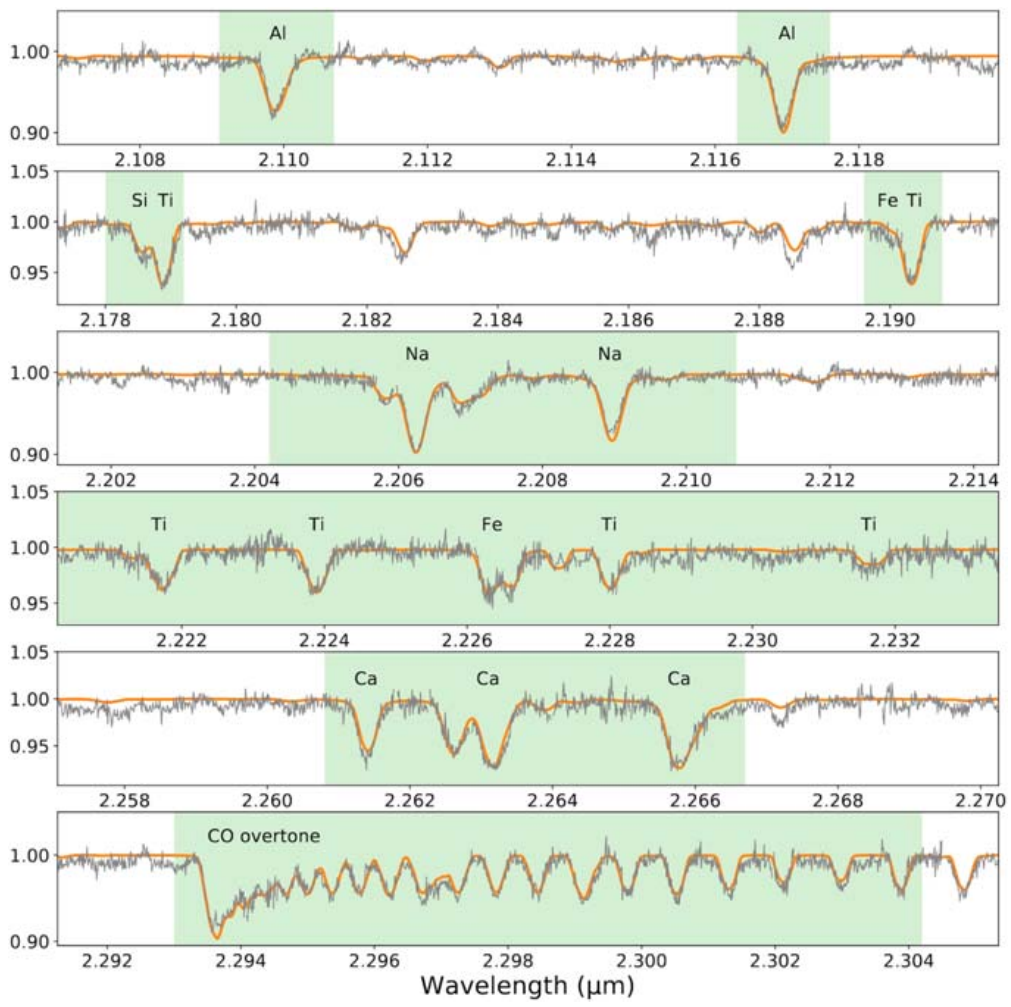


Figure 20. Comparison between the observed spectrum of T Tauri North observed in *K2* mode (in gray) and 0.″75 slit ($R \approx 49{,}000$), and a best-fit model (in orange). The eight green shaded regions show the wavelength regions used to fit the spectrum of the young star. The S/N is about 200 per pixel. From Flores et al. (2020).

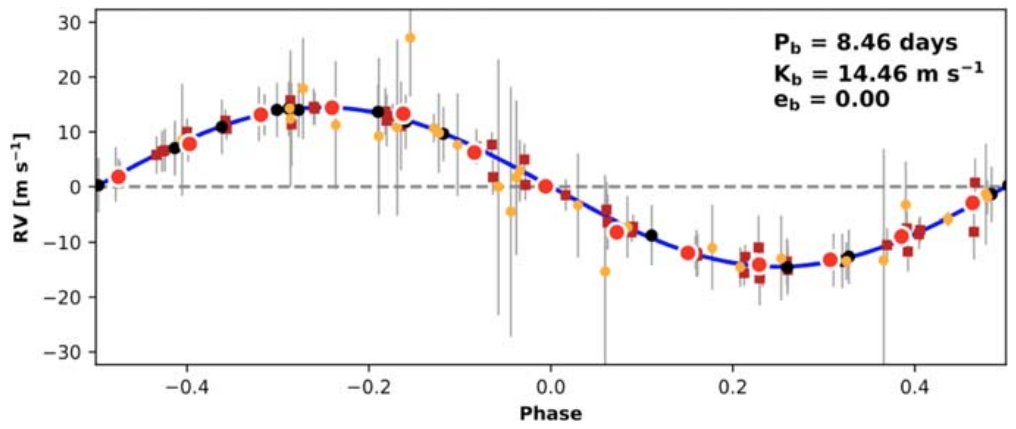


Figure 21. RV measurements phased to the orbital period of AU Mic b. The data come from three spectrographs: iSHELL (yellow circles), HIRES (black circles) and HARPS (red squares). The 1σ uncertainties for iSHELL are about 15 ms^{-1}. The blue curve is the best fit to the orbit after subtracting the best fit model of stellar activity. See Plavchan et al. (2020).

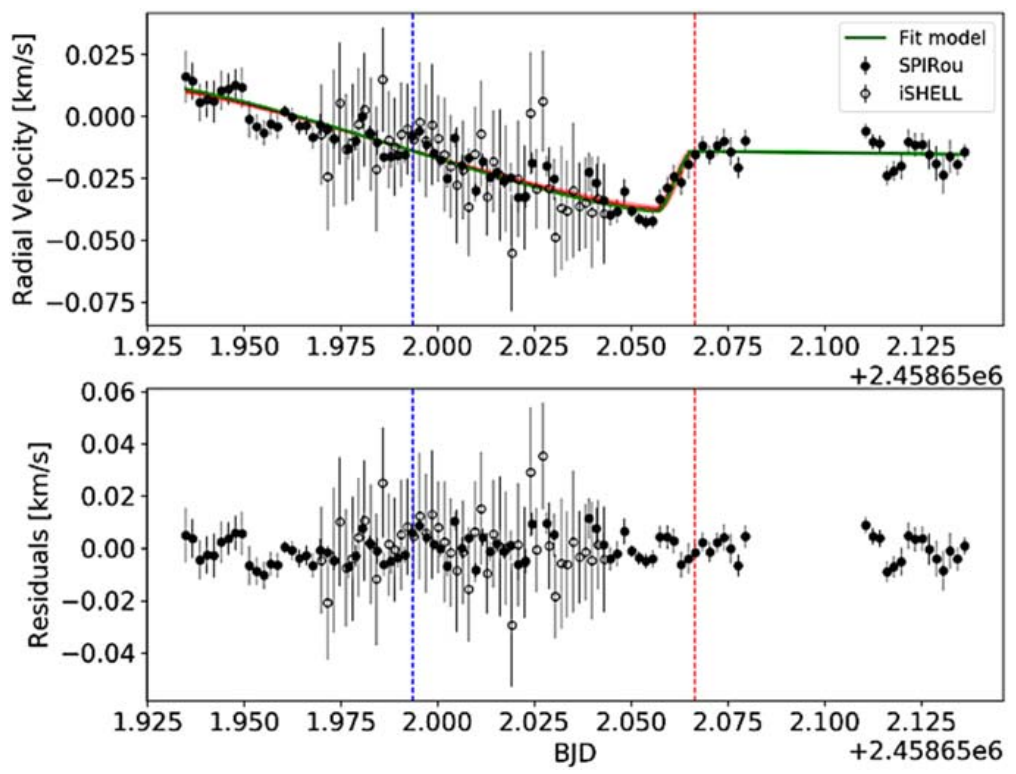


Figure 22. Simultaneous fit to the SPIRou RVs and iSHELL RVs of the model of the Rossiter-McLaughlin effect from Martioli et al. (2020). The vertical dashed lines show the predicted transit center (blue) and end (red). iSHELL did not observe the end of the transit. Bottom panel: residuals of the fit with respective dispersions of 5.1 m s^{-1} and 11.5 m s^{-1} for SPIRou and iSHELL respectively. The higher dispersion in the iSHELL data is due to the narrower one-shot wavelength range of iSHELL, slit losses and smaller aperture telescope compared to the fiber-fed SPIRou on CFHT.

independent techniques for data analysis is "remarkable" and shows that both instruments are stable and can provide short-term RVs with precisions of a few m s^{-1} for an active star.

High resolution spectral observations of comets at 3–5 μm is an important niche for IRTF. IRTF is unique for an optical-infrared telescope in regularly conducting daytime observations, which is particularly valuable for the perihelion passage of comets. An important factor in finding and guiding on daytime comets near perihelion is imaging in a thermal filter (narrow-band *L*, see inset Figure 23).

A good example are the iSHELL observations of the Oort cloud comet C/2017 E4 (Lovejoy) by Faggi et al. (2018) as it approached Earth in early April 2017, and before its disruption just after perihelion in late April. Twelve molecular species were identified: nine primary volatiles (H_2O, HCN, NH_3, CO, C_2H_2, C_2H_6, CH_4, CH_3OH, H_2CO) and three product species (CN, NH_2, OH). Examples of the data are shown in Figure 23.

Melin et al. (prep). are using iSHELL in the *Lp4* mode with the 0.″375×25.″0 to probe the polar auroral regions of Jupiter through H_3^+ emission spectra to measure the temperature and ion densities of the upper atmosphere. By scanning the slit across the polar region, temperature is mapped every 25 minutes (see Figure 24). The 25.″0 slit was added to iSHELL specifically for Jupiter H_3^+ observations. The observations are coordinated with Juno observations.

During iSHELL commissioning Brittain et al. (2018) observed the Herbig Ae star HD 179218 (magnitude $M = 3.95$) as a test for the instrument's spectro-astrometry performance. The spectro-astrometry technique (e.g., Whelan & Garcia 2008) is sensitive to spatial scales orders of magnitude less than the seeing. The star was observed in the *M2* mode at 5 μm and the 0.″375 slit ($R = 88{,}100$) for 30 min with a 0.″6 PSF (seeing plus guiding). The broad one-shot spectral grasp provides simultaneous observations of many CO lines. Stacking these lines significantly improves the S/N of the line profile and the spectro-astrometric signal. The resulting CO $v = 1$–0-line profile shown in Figure 25 is the average of 48

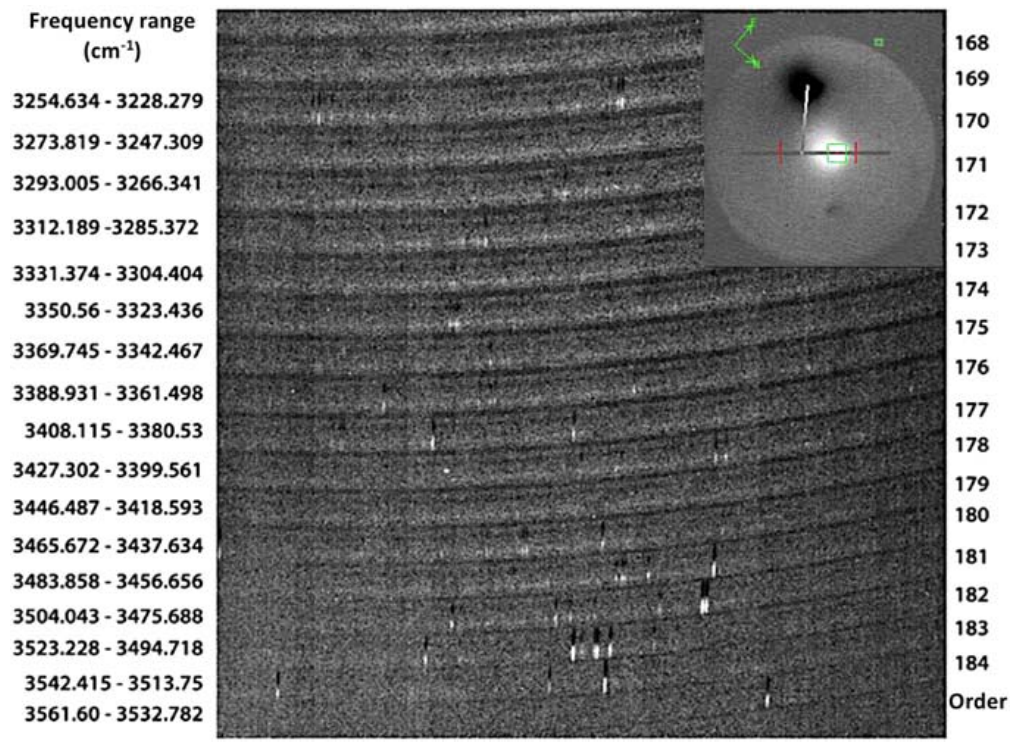


Figure 23. Daytime spectral image of comet C/2017 E4 (Lovejoy) in the *L1*-custom mode (2.81–3.11 μm, see Table 1) showing many H_2O lines. The comet is nodded within the slit to subtract the sky. The inset (top-right) shows the slit viewer image in the narrow-band L 3.46 μm filter used for daytime acquisition and guiding. The guide box is in green and the red bars show the extent of the $0\farcs75 \times 15\farcs0$ slit used ($R \approx 49{,}000$). From Faggi et al. (2018).

transitions, resulting in a S/N along the continuum of 520, and the standard deviation of the centroid measurement is 0.44 mas. The ETC[28] and delivered signal are found to be consistent with expectations to within about 10% near the peak of the grating blaze.

Abernathy et al. (2021) are conducting a survey of high-resolution CO rovibrational *M*-band spectra in Herbig Ae/Be disks. With iSHELL this coverage includes part of the rovibrational R band and the entire P branch of the CO fundamental band ($\Delta v = 1$–0), one of the best tracers of warm gas in protoplanetary disks (see Figure 26). Analysis reveals structures and cavities in inner disk regions.

The 5 μm spectrum of Jupiter preserves the signature of the deep atmosphere via pressure-broadened line shapes, which are fully resolved at iSHELL resolving powers. Observations in the *M1* mode at $R \approx 49{,}000$ ($0\farcs75 \times 15\farcs0$ slit) by Bjoraker et al. (2018) of water cloud-top altitudes in the GRS, combined with CO measurements, have constrained Jupiter's O/H ratio to be between 2 and 9 times solar. This is in excellent agreement with the Juno Microwave Radiometer (MRW) value of 1 to 5 times solar at the equator and it is independent of the technique used by the MWR team (Li et al. 2020).

Accurate slit placement was accomplishing by guiding on a 5 μm "hot spot" visible in the slit-viewer 5.1 μm narrow-band filter (see Figure 27). Since the hot spot is rotating at the Jovian rotation rate, the slit tracks the same longitudes as Jupiter rotates. Context imaging with the slit is also very valuable for planetary atmospheres. The combination of excellent seeing and low water vapor resulted in high quality spectra of Jupiter (see Figure 28).

[28] irtfweb.ifa.hawaii.edu/~ishell/iSHELL_Exposure_Time_Calculator/

10. Lessons Learned

The performance of the silicon immersion grating (SIG) fabricated by UT is excellent (e.g., see Figure 9). One significant surprise is that silicon has useful transmission shorter than expected, down to at least 1.06 μm at 80 K. The cut-off wavelength was known to get shorter with decreasing temperature. However, the limit seems to be about 1.04 μm at 4 K (Macfarlane et al. 1958) and so there is little to be gained by cooling silicon below about 80 K.

Cale et al. (2019) claimed that the SIG in iSHELL introduced variable frequency fringing. However, subsequent analysis has shown that this effect was an artifact introduced by the radial velocity measurement code being used (Plavchan priv. comm). and was not introduced by the SIG. The overall performance of the SIGs in both iSHELL and IGRINS augurs well for further instruments based on this technology.

At the time iSHELL was being designed and built UT was only able to fabricate one SIG for the project. As explained in Section 2, this has resulted in compromises to the one-shot wavelength coverage and slit length. To better match the free spectral range to the width of the array, ideally more SIGs, each optimized for the wavelength range of interest, are required to cover 1–5 μm (e.g., as proposed in UT instruments for Magellan and the Grand Magellan Telescope). To allow for a possible future upgrade, additional space has been left for a 1–2.5 μm optimized SIG on the optical bench.

Fringing is observed in flat fields with a contrast of about 5%. The spatial frequency of the fringing varies linearly with wavelength from about 20 pixels at *J* to about 70 pixels at *M*. The fringe intensity does not vary in the spatial direction along the slit and is tilted slightly with respect to detector columns, the same as arc lines (see Section 4.3). Typically, fringing is produced by interference in parallel-sided optical substrates. From Born & Wolf (1980) the fringe period in wavelength, $\delta\lambda$, is given by

$$\partial\lambda = \frac{\lambda^2}{2\mathcal{F}nh} \text{ with finesse } \mathcal{F} = \frac{\pi\mathcal{R}^{1/2}}{1-\mathcal{R}}$$

where λ is the wavelength, n is the refractive index of the substrate, h is the thickness of the substrate, and $\mathcal{R}$ the internal reflectivity of the substrate. From this formulation the observed fringe spatial frequencies are roughly consistent with low internal reflectivity ($\mathcal{F} \sim 1$) in optical substrates about one cm thick. Potential culprits in iSHELL are the order-sorting filters, slit and window substrates. However, we have been able to eliminate all these possibilities. Wedging the filters has had no effect and the slit substrates are tilted such that interfered beams are absorbed by the backside metal absorption coating (see Section 4.6). A ZnSe substrate placed in optical contact with

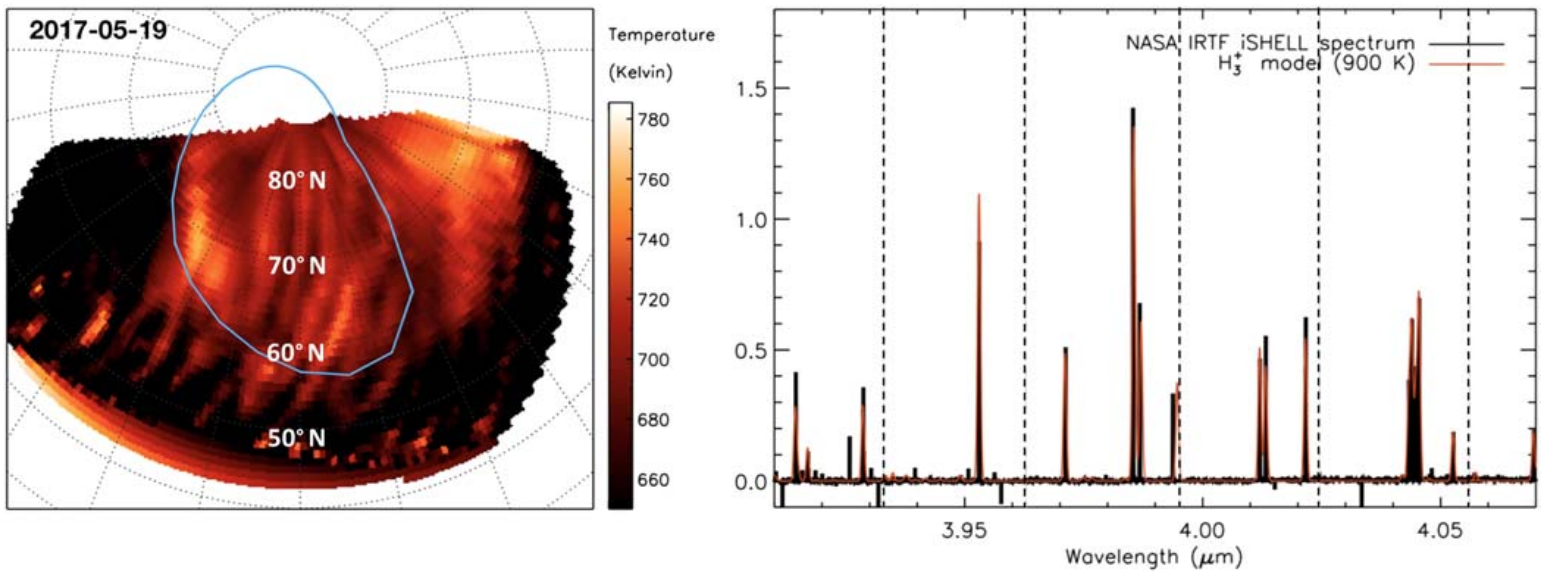


Figure 24. (Left) The $0\farcs375 \times 25''$ slit in *Lp4* mode was scanned across of the northern auroral region of Jupiter using an observing macro procedure, forming a high-resolution H_3^+ spectral image. A total of 25 slit positions was used, each with a 30 second exposure, achieving a high temporal cadence view of the thermal morphology of the polar region. The grey line indicates the average location of the main auroral oval as observed by the Hubble Space Telescope. (Right) An example Jupiter auroral spectrum ($R \approx 80{,}000$) taken on 19 May 2017, showing six spectral orders containing strong H_3^+ lines and a H_3^+ spectral model at 900 K. The boundary between spectral orders are separated by grey dashed lines. Melin et al. (2021 in preparation).

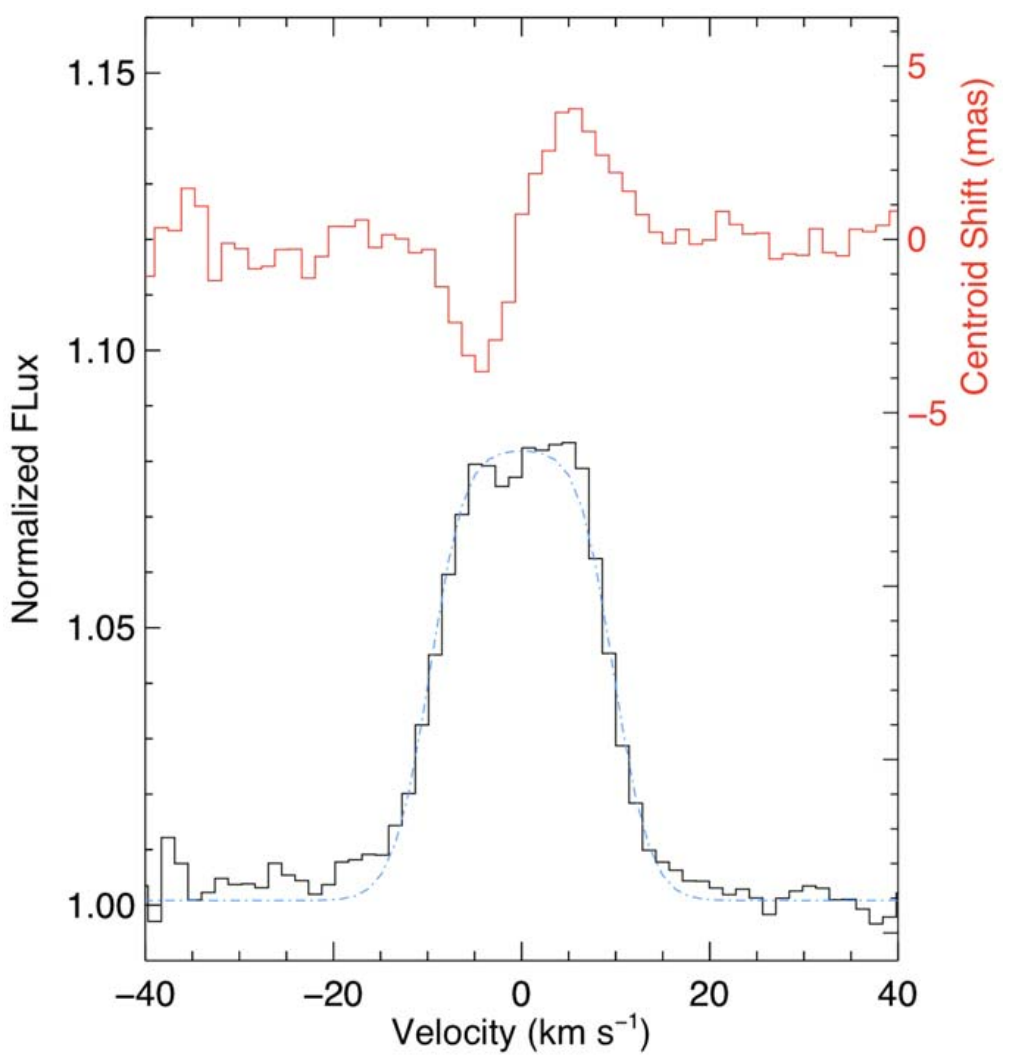


Figure 25. Profile of v = 10 CO lines and spectro-astrometric signal from Brittain et al. (2018) for HD179218. The FWHM of the emission line is 19.51 ± 0.27 km s^{-1} and the centroid shift of the line profile is consistent with a 15 au radius Keplerian disk (allowing for optical depth effects).

the warm cryostat entrance window also had no effect on the fringe frequency and contrast as would be expected if the window was the source. Also, the H2RG detector is substrate removed, and so cannot cause fringing. One source of fringing that we have not been able to eliminate is the multiple layer dielectric anti-reflection coatings on the refractive optics. It is speculation but the thin dialectic layers coupled with the high finesse could possibly produce resolved fringing in a high-resolution spectrograph.

Due to a small amount of flexure in the instrument, the fringing does not divide out perfectly. In flats taken an hour apart as the telescope tracks and changes the gravity vector, a flat field residual of about 1% remains (resulting from 1–2 pixels of movement in the dispersion direction). For spectral features at the spatial frequency of the fringes (20–70 pixels depending on wavelength) this limits the S/N to about 100. For observing programs requiring better S/N at these scales, calibration can be done more frequently. However, narrower spectral features are minimally affected. The most likely source of the flexure is very slight rotation in the cross-dispersing grating turret, where the turret is held in place by the detented mechanism. Positioning of the turret is highly sensitive due to the very long optical lever arm (one pixel of movement results from 30″ of rotation).

Integrating spheres have excellent spatial scrambling properties but as a consequence, transmissions of only a few percent. As a result, we now use the low-pressure Th-Ar lamp in position directly over the cryostat entrance window but with somewhat compromised spatial scrambling (see Figure 2 and Section 4.8). A better approach might be to use a diffuser design (transmission about 40%) of the type built for the Gemini Calibration system (Ramsay-Howat et al. 2000) if it could be fitted into the smaller space available on IRTF. Due to the increasing opacity and the resulting thermal emission from the quartz envelope of the commercial HCL Th-Ar lamp used in iSHELL, we have successfully used the rich telluric spectrum for 3–5 μm wavelength calibration.

There are two upward-looking hermetic circular 50-pin mil spec connectors on the bottom of the cryostat, one for the spectrograph array clock/bias signals and one for the spectrograph array analog output signals (see Figure 29). During commissioning we experienced an electrical short at the

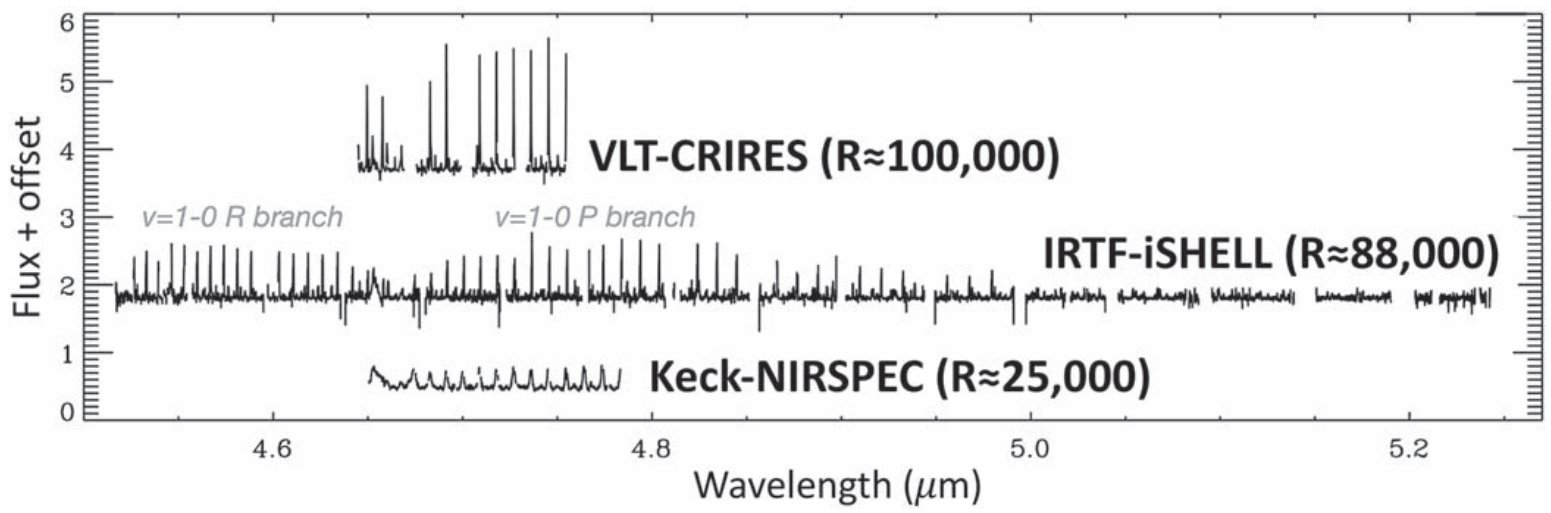


Figure 26. The broad one-shot wavelength coverage of iSHELL in the *M*-band compared to CRIRES and NIRSPEC. The wide grasp allows many CO lines to be stacked, significantly improving S/N of the line profile. (CRIRES has recently been upgraded to a cross-dispersed format to increase its one-shot wavelength coverage). From Abernathy et al. (2021).

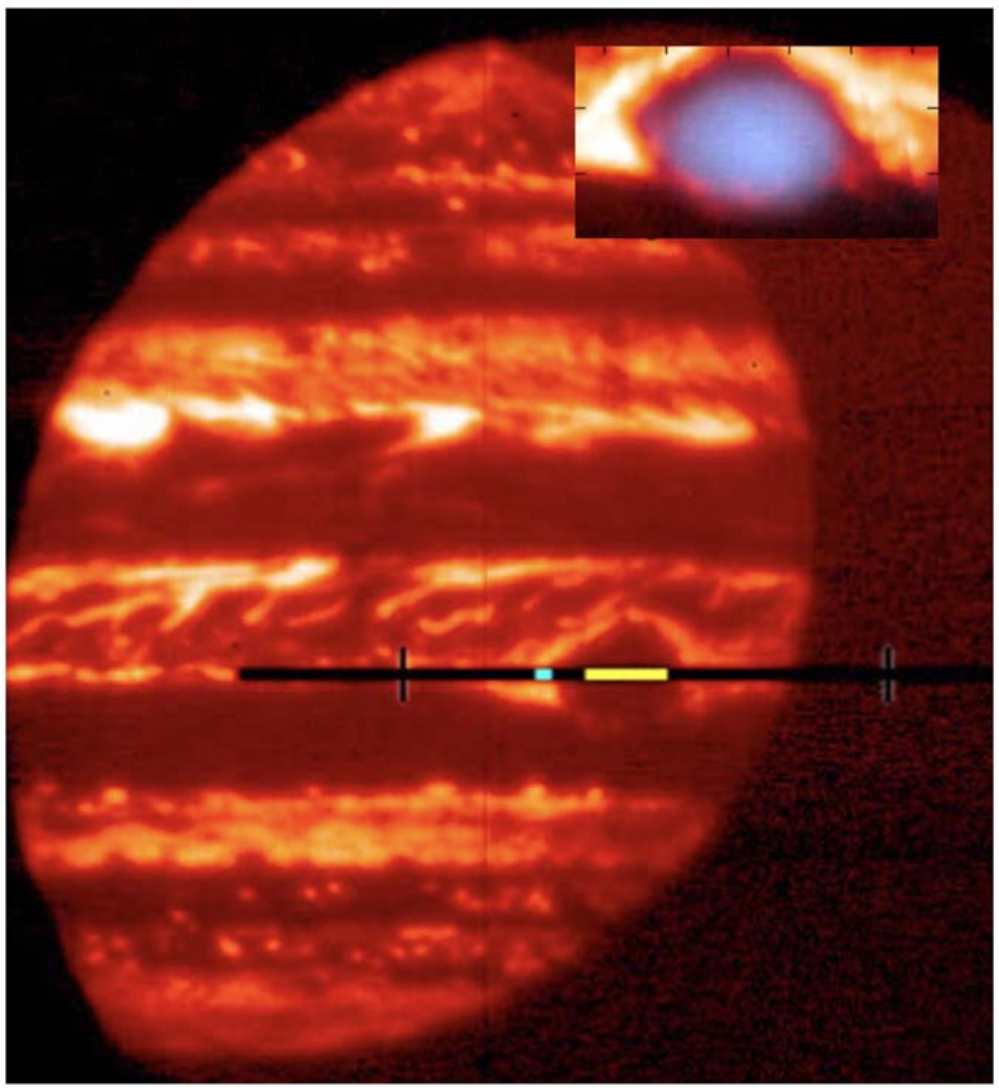


Figure 27. Image of Jupiter and the Great Red Spot (GRS) at 5.1m using the slit-viewing camera (a subset of the image is shown here). The GRS is dark due to thick clouds that block thermal radiation. Yellow pixels denote the portion of the GRS that is used in the analysis. The inset (top-right) is a composite image of the GRS at 2.2 μm (blue) and at 5.1 m using the slit-viewing camera. The GRS is bright in the 2.2 μm methane-band images due to upper tropospheric haze. Cyan pixels show the location of the Warm Collar spectrum west of the GRS (see Figure 28). From Bjoraker et al. (2018).

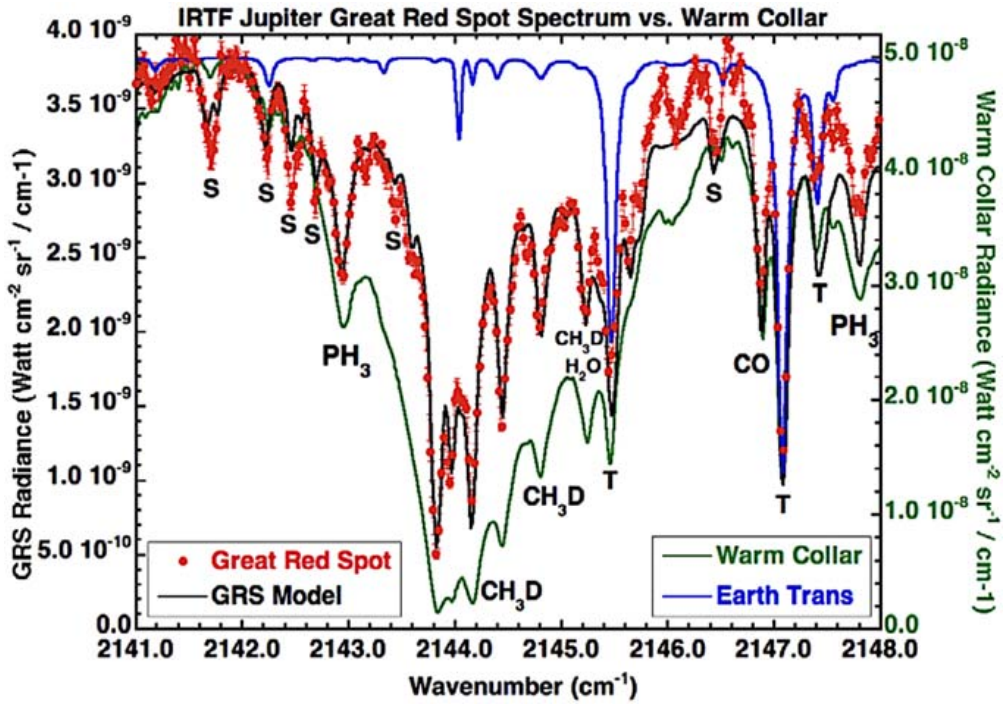


Figure 28. Comparison between $R \approx 49{,}000$ spectra of the GRS (red, left-hand axis) and of the Warm Collar (green, right-hand axis) at 4.66 μm. The Warm Collar is 13 times brighter than the GRS. The best fitting model of the GRS and a model of the transmittance of the atmosphere above Maunakea are also shown (blue). The transmittance scale (not shown) is 0–1.04. Telluric lines are denoted by T and solar lines by S. From Bjoraker et al. (2018).

clock/bias pin-out due to a small flake of aluminum debris across a couple of the pins. No permanent damage was done and we installed covers over both connectors to avoid further incidents. In future we will avoid using upward-looking connectors on cryostats. Despite employing clean room procedures, a small amount of internal debris was created during assembly with the mutiple fasterners used on the cold bench and radiation shields, both of which are too large for the ultra-sonic cleaning employed on the smaller assemblies. In future, to mitigate against the creation of small flakes and ganular debris from bolted interfaces, we will also use more helicoil inserts, and more carefully examine and clean blind bolt holes.

As was found to be the case for the facility 0.8–5.4 μm $R = 50$–2500 spectrograph, SpeX, the ability to acquire and guide on targets across the 1–5 μm range, has proved very valuable for iSHELL. Examples include, optical targets at *J*, embedded targets at *K*, daytime guiding on comets at narrow-band *L*, and guiding on planetary features at narrow-band *M*. Simultaneous spectroscopy and context imaging of planetary atmospheres has also significantly improved science return.

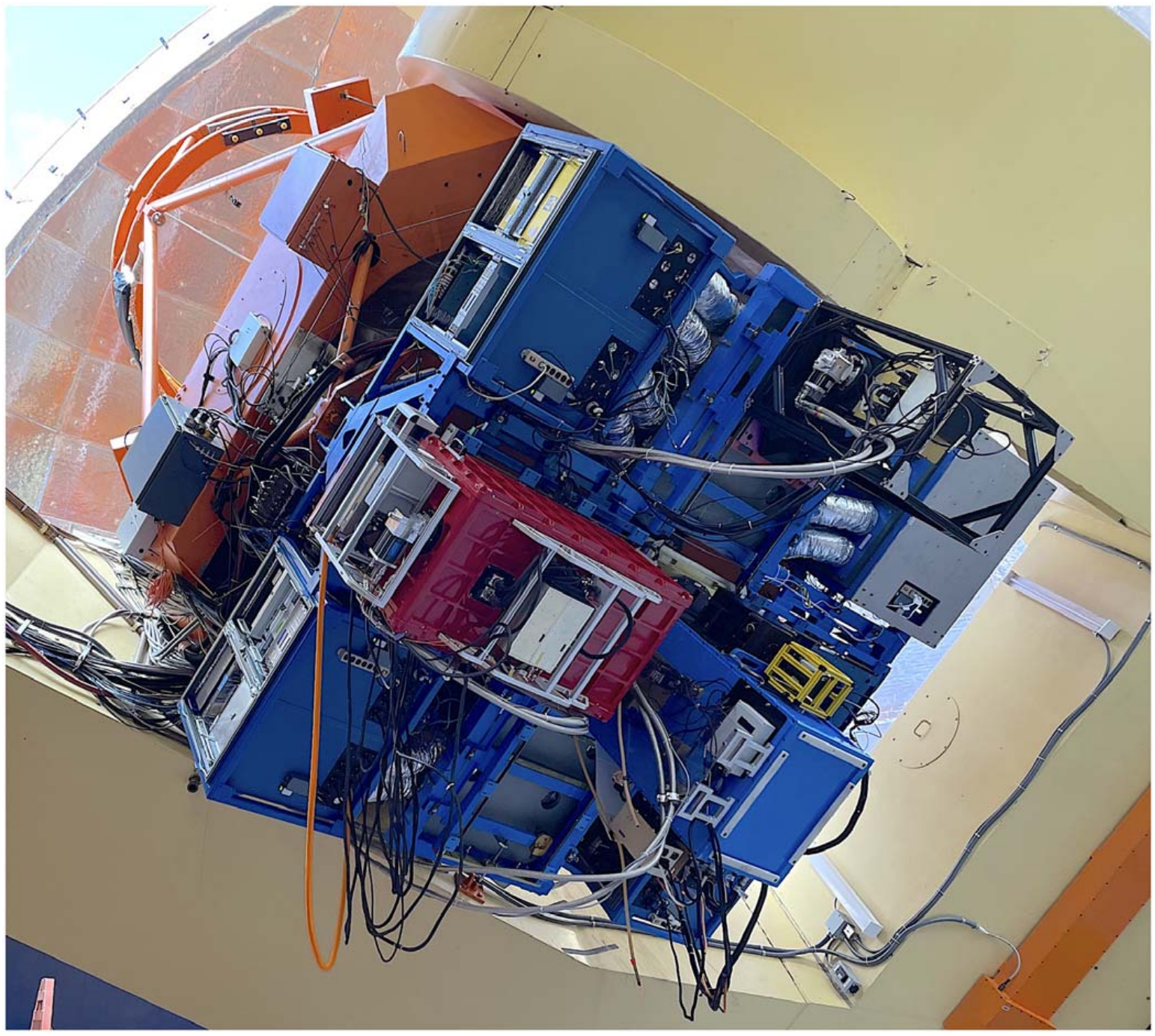


Figure 29. iSHELL (red) pictured in the north instrument stow position on IRTF. Note the spectrograph H2RG array controller box mounted on the bottom of iSHELL, together with the two upward-looking connectors. The other instruments also mounted on the multiple instrument mount are SpeX (blue, on-axis) and the mid-IR instrument, MIRSI, in the west stow position (top-right). The blue boxes above the instruments house cooled electronics for the instruments.

The use of a pupil viewer in the slit viewer has turned out to be very beneficial. First, as intended, to align the instrument with the telescope entrance pupil (the secondary mirror). In the past this was a time-consuming procedure that peaked up on the signal from a star and minimized the thermal signal from the telescope by shimming the instrument at the telescope mount. The second benefit has been to identify and fix flexure in the telescope interface above the instrument, namely movement in the bearings on the telescope instrument rotator, which SpeX and iSHELL no longer need due to their built-in image rotators.

Figure 29 shows iSHELL mounted to the telescope together with the two other facility instruments, SpeX and MIRSI.

We acknowledge the support of NSF award AST-0821866 for building iSHELL, NSF collaborative award AST-1407797 for iSHELL data reduction, NASA Contract numbers NNH14CK55B (2014–2018) and 80HQTR19D0030 (2019–2024) for IRTF operations, and the University of Hawaii. Building iSHELL was a team effort and we thank all members of the IRTF staff. In particular the day crew—Lars Bergknut, Paul Berrios, Maury McOuat, Imai Namahoe, Kyle Usui and Darryl Watanabe, the telescope operators—Brian Cabreira, Greg Engh, Dave Griep, Tony Matulonis, Greg Osterman and Bernie Walp, and staff engineers Tony Denault, Miranda Hawarden-Ogata, Mike Keli'i and Jessica Young. Graduate student Christian Flores and support astronomer Adwin Boogert, measured iSHELL's spectral line spread function. In-house mechanical fabrication was handled by Lou Robertson and Paul Toyama at the IfA Manoa machine shop. Financial matters were managed by Sandra Miyata and Amy Shimabukuru. iSHELL would not have been possible without the personnel at UT involved in the decade-long development of the silicon immersion grating technology. The iSHELL preliminary design review was conducted by Jay Elias (chair), Dan Jaffe, Mike Mumma, Peter Onaka, Doug Tommey and David Warren. Help with the science case was provided by Gordy Bjoraker, John Carr, Neil Dello Russo, Mike DiSanti, Chris Johns-Krull, Steve Miller, Mike Mumma, Joan Najita, Bob Novak, Peter Plavchan and Lisa Prato. Mike Mumma was PI for the project that procurred the InSb guide arrays used in both SpeX and iSHELL. We also thank Christ

Ftaclas for educating us about stray light and Power Spectrum Density analysis.

Finally, it was an honor for the IRTF staff to work with Don Hall. Among many other things, Don led the development of the HAWAII series of arrays at UH. His guidance and support is missed by all.

The authors wish to recognize and acknowledge the very significant cultural role and reverence that the summit of Maunakea has always had within the indigenous Hawaiian community. We are most fortunate to have the opportunity to conduct observations from this mountain.

We thank the anonymous referee for a very thorough and beneficial review of this paper.

ORCID iDs

John Rayner https://orcid.org/0000-0002-3165-159X
Alan Tokunaga https://orcid.org/0000-0001-8136-9704
Michael Connelley https://orcid.org/0000-0002-8293-1428
Michael Cushing https://orcid.org/0000-0001-7780-3352
William Vacca https://orcid.org/0000-0002-9123-0068

References

Abernathy, K. M., Banzatti, A., Jensen, S., et al. 2021, RNAAS, 5, 80
Baranne, A. 1972, in Proc. of ESO/CERN conference on auxiliary Instrumentation for large telescopes, 227
Banzatti, A, et al. 2022, AJ, submitted
Bjoraker, G. L., Wong, M. H., de Pater, I., Hewagama, T., Ádámkovics, M., et al. 2018, AJ, 156, 101
Born, M., & Wolf, E. 1980, Principles of Optics, Sixth (Corrected) Edtion (Pergamon Press)
Brittain, S. D., Carr, J. S., & Najita, J. R. 2018, PASP, 130, 074505
Cale, B., Plavchan, P., LeBrun, D., et al. 2019, AJ, 158, 170
Cushing, M. C., Vacca, W. D., & Rayner, J. T. 2004, PASP, 116, 362
Donati, J.-F., Kouach, D., Moutou, C., et al. 2020, MNRAS, 498, 5684
Engleman, R., Hinkle, H. K., & Wallace, W. 2003, JQSRT, 78, 1
Faggi, S., Villanueva, G. L., Mumma, M. J., & Paganini, L. 2018, AJ, 156, 68
Flores, C., Reipurth, B., & Connelley, M. S. 2020, AJ, 898, 109
Fowler, A. M., & Gatley, I. 1990, ApJ, 353, L33
Greene, T. P., Tokunaga, A. T., Toomey, D. W., & Carr, J. B. 1993, Proc. SPIE, 1946, 313
Groh, J. H., Damineli, A., & Jablonski, F. 2007, A&A, 465
Gully-Santiago, M., Wang, W., Deen, C., & Jaffe, D. 2012, Proc. SPIE, 8450, 84502S
Jones, H. R. A., Rayner, J., Ramsey, L., et al. 2012, Proc. SPIE, 7014, 701407
Kelson, D. D. 2003, PASP, 115, 688
Kerber, F., Nave, G., & Sansonetti, C. J. 2008, ApJS, 178, 374
Kvamme, E. T., Trevias, D., Simonson, R., & Sokolsky, L. 2005, Optomechanics, 5877, 276
Lacy, J. H., Richter, M. J., Greathouse, T. K., Jaffe, D. T., & Zhu, Q. 2002, PASP, 114, 153
Li, C., Ingersoll, A., Bolton, S., et al. 2020, NatAs, 4, 609
Lord, S. D. 1992, A New Software Tool for Computing Earth's Atmospheric Transmission of Near- and Far-Infrared Radiation, NASA Tech, Mem., 103957 (Washington, DC: NASA)
Macfarlane, G. G., McLean, T. P., Quarrington, J. E., & Roberts, V. 1958, PhRv, 111, 1245
Maihara, T., Iwamuro, F., Yamashita, T., et al. 1993, PASP, 105, 940
Marsh, J. P., Mar, D. J., & Jaffe, D. T. 2007, ApOpt, 46, 3400
Martioli, E., Hébrard, G., Moutou, C., et al. 2020, Astronomy and Astrophysics, 641, L1
McCaughrean, M. J. 1988, Ph.D. Thesis, Univ. of Edinburgh, UK
Mumma, M. J., Villanueva, G. L., Novak, R. E., et al. 2009, Sci, 323, 1041
Nave, G., Kerber, F., Den Hartog, E. A., & Lo Curto, G. 2018, Proc. SPIE, 10704, 1070407
Nave, G., Shlosberg, A., Redman, S. L., & Sansonetti, C. J. 2008, https://www.nist.gov/pml/spectrum-th-ar-hollow-cathode-lamps
Park, C., Jaffe, D. T., Yuk, I.-S., et al. 2014, Proc. SPIE, 9147, 91471D
Plavchan, P., Barclay, T., Gagné, J., et al. 2020, Nature, 582, 497
Ramsay-Howat, S. K., Harris, J. W., Gostick, D. C., et al. 2000, Proc. SPIE, 4008, 1351
Rayner, J., Bond, T., Bonnet, M., et al. 2012, Proc. SPIE, 8446, 84462C
Rayner, J., Tokunaga, A., Jaffe, D., et al. 2016, Proc. SPIE, 9908, 990884
Rayner, J. T., Toomey, D. W., Onaka, P. M., et al. 2003, PASP, 115, 362
Regan, M. W., & Bergeron, L. E. 2020, JATIS, 6, 016001
Robertson, J. G. 2013, PASA, 30, 48R
Schroeder, D. J. 2000, Astronomical Optics (San Diego: Academic Press)
Snellen, I. A. G., de Kok, R. J., de Mooij, E. J. W., & Albrecht, S. 2010, Natur, 465, 1049
Stover, J. C. 1990, Optical scattering: measurement and analysis (New York: McGraw-Hill)
Sullivan, P. W., & Simcoe, R. A. 2012, PASP, 124, 1336
Tokunaga, A. T., Toomey, D. W., Carr, J., Hall, D. N. B., & Epps, H. W. 1990, Proc. SPIE, 1235, 131
Tull, R. G., MacQueen, P. J., Sneden, C., & Lambert, D. L. 1995, PASP, 107, 251
Vacca, W. D., Cushing, M. C., & Rayner, J. T. 2003, PASP, 115, 389
Vacca, W. D., Cushing, M. C., & Rayner, J. T. 2004, PASP, 116, 352
Wang, W., Gully-Santiago, M., Deen, C., Mar, D. J., & Jaffe, D. T. 2010, Proc. SPIE, 7739, 77394L
Whelan, E., & Garcia, P. 2008, Jets from Young Stars II, 742, 123